Available online at www.sciencedirect.com

ScienceDirect

Geochimica et Cosmochimica Acta 189 (2016) 338–358

Geochimica et Cosmochimica Acta

www.elsevier.com/locate/gca

CV and CM chondrite impact melts

Nicole G. Lunning [a,b,*], Catherine M. Corrigan [b,1], Harry Y. McSween Jr. [a,2], Travis J. Tenner [c,d,3], Noriko T. Kita [c,4], Robert J. Bodnar [e,5]

[a] Department of Earth and Planetary Sciences and Planetary Geosciences Institute, University of Tennessee, Knoxville, TN 37996, USA
[b] Department of Mineral Sciences, Smithsonian Institution, National Museum of Natural History, Washington, DC 20560, USA
[c] Department of Geosciences, University of Wisconsin, Madison, WI 53706, USA
[d] Chemistry Division, Nuclear and Radiochemistry, Los Alamos National Laboratory, MSJ514, Los Alamos, NM 87545, USA
[e] Department of Geosciences, Virginia Tech, Blacksburg, VA 24061, USA

Received 28 July 2015; accepted in revised form 25 May 2016; Available online 3 June 2016

Abstract

Volatile-rich and typically oxidized carbonaceous chondrites, such as CV and CM chondrites, potentially respond to impacts differently than do other chondritic materials. Understanding impact melting of carbonaceous chondrites has been hampered by the dearth of recognized impact melt samples. In this study we identify five carbonaceous chondrite impact melt clasts in three host meteorites: a $CV3_{red}$ chondrite, a $CV3_{oxA}$ chondrite, and a regolithic howardite. The impact melt clasts in these meteorites respectively formed from $CV3_{red}$ chondrite, $CV3_{oxA}$ chondrite, and CM chondrite protoliths. We identified these impact melt clasts and interpreted their precursors based on their texture, mineral chemistry, silicate bulk elemental composition, and in the case of the CM chondrite impact melt clast, *in situ* measurement of oxygen three-isotope signatures in olivine. These impact melts typically contain euhedral–subhedral olivine microphenocrysts, sometimes with relict cores, in glassy groundmasses. Based on petrography and Raman spectroscopy, four of the impact melt clasts exhibit evidence for volatile loss: these melt clasts either contain vesicles or are depleted in H_2O relative to their precursors. Volatile loss (i.e., H_2O) may have reduced the redox state of the CM chondrite impact melt clast. The clasts that formed from the more oxidized precursors ($CV3_{oxA}$ and CM chondrites) exhibit phase and bulk silicate elemental compositions consistent with higher intrinsic oxygen fugacities relative to the clast that formed from a more reduced precursor ($CV3_{red}$ chondrite). The mineral chemistries and assemblages of the CV and CM chondrite impact melt clasts identified here provide a template for recognizing carbonaceous chondrite impact melts on the surfaces of asteroids.

Keywords: Impact melt; Carbonaceous chondrite; CV chondrite; Howardite; CM chondrite; Vesta; Regolith; Oxygen isotopes; Relict olivine; Melt spherule; Melt pocket; Melt clast

* Corresponding author at: Department of Mineral Sciences, Smithsonian Institution, P.O. Box 37012, MRC 119 Washington, DC 20013-7012, USA. Tel.: +1 (202) 633 1865.

E-mail addresses: lunningn@si.edu (N.G. Lunning), corriganc@si.edu (C.M. Corrigan), mcsween@utk.edu (H.Y. McSween), tenner@lanl.gov (T.J. Tenner), noriko@geology.wisc.edu (N.T. Kita), rjb@vt.edu (R.J. Bodnar).

[1] Tel.: +1 (202) 633 1855.
[2] Tel.: +1 (865) 974 9805.
[3] Tel.: +1 (505) 664 0115.
[4] Tel.: +1 (608) 262 7118.
[5] Tel.: +1 (540) 231 7455.

http://dx.doi.org/10.1016/j.gca.2016.05.038
0016-7037/

1. INTRODUCTION

The effects of impacts onto most carbonaceous chondrite targets are not well understood. Only a few impact melts have been reported in carbonaceous chondrites, an observation which led Scott et al. (1992) to speculate that volatile components (e.g., H_2O, CO_2, S_2) in carbonaceous chondrites would respond to impact shocks explosively and prevent the formation of impact melt. CK chondrites were the exception in that at least three samples contain opaque shock veins (Rubin, 1992). CK chondrites are notably different from other carbonaceous chondrite groups, as they have typically experienced a greater extent of thermal metamorphism, after which some were exposed to impacts that shock-blackened silicates (Kallemeyn et al., 1991). This work will examine potential impact melts of CV and CM chondrites. It has been suggested that CV and CK chondrites come from the same parent body based on similarities in their bulk isotopic and element compositions (Greenwood et al., 2010; Wasson et al., 2013). However, differences in the mineral chemistries and calculated intrinsic fO_2 between the CV and CK chondrites cannot parsimoniously reconcile these two carbonaceous chondrite groups into a metamorphic suite akin to those of the type 3–6 ordinary chondrites (Righter and Neff, 2007; Dunn et al., 2015).

The Leoville CV3 chondrite contains a ~100 μm area of quenched microporphyritic olivine in glass that was initially interpreted as melt generated by an accretionary collision (Caillet et al., 1993). An alternative interpretation is that the melt formed after assembly of the CV parent body. We characterize impact melts in three host meteorites: RBT 04143 ($CV3_{red}$) chondrite, LAR 06317 ($CV3_{oxA}$) chondrite, and GRO 95574 (regolithic howardite) and argue that they were derived from precursors that prior to impact melting had experienced only low-temperature thermal metamorphism and/or aqueous alteration.

Carbonaceous chondrites are generally expected to respond to impact shocks in a manner similar to that of ordinary chondrites (Scott et al., 1992). In this regard, the numerous descriptions of ordinary chondrite impact melts (e.g., Rubin, 1985; Bogard et al., 1995) provide useful references when considering impact melting of chondritic material. In ordinary chondrites, impact melt clasts typically have bulk elemental compositions that are similar to the material from which they melted (Dodd et al., 1982; Bogard, 2011). Only very small degrees of partial melting (producing feldspathic melt pockets) due to impacts have been observed in ordinary chondrites (Dodd and Jarosewich, 1982). This is consistent with shock effects for porous rocks (e.g., chondrites) described by Bischoff and Stöffler (1992): highly localized, incipient partial melting is immediately succeeded by complete bulk melting without intermediate partial melting. Differences between impact melt compositions and the major element bulk compositions of their protoliths are usually explained by processes that occurred after bulk melting. For example, loss of volatiles or separation of immiscible sulfide-metal liquids from the silicate melt fraction will change the bulk elemental composition in ways that can be anticipated (Bogard et al., 1995; Mittlefehldt and Lindstrom, 2001). In addition to impact melts generated *in situ* by shock waves propagating through the target material (e.g., Dodd and Jarosewich, 1982; Benedix et al., 2008), impact-related melting can also occur at the interface between the impactor and target (i.e., on the floors of impact craters), or melts can be ejected as molten droplets. These melts can form exclusively from target material, a mixture of the target and impactor material, or exclusively from impactor material (e.g., Symes et al., 1998; Asphaug et al., 2011; Udry et al., 2014; Johnson et al., 2015; Fazio et al., 2016).

Differences between ordinary and carbonaceous chondrites—specifically CV and CM chondrites—might lead to certain distinct responses to impacts:

(1) All ordinary chondrite chemical groups include members that have experienced relatively high-temperature thermal metamorphism (petrologic type > 4). In contrast, there are no widely accepted CV or CM chondrites of petrologic type > 4, meaning their mineral assemblages are either unequilibrated or partially equilibrated at relatively low temperatures.
(2) Compared to ordinary chondrites, CV and CM chondrites have higher intrinsic oxygen fugacities (Rubin et al., 1988) and more frequently contain forms of water (Wasson and Kallemeyn, 1988; Jarosewich, 1990). Carbonaceous chondrites contain between 0 and 18 wt.% water-equivalent hydrogen, and CV and CM chondrites respectively contain 0–2.5 wt.% and 6.5–12.5 wt.% water-equivalent hydrogen (Wasson and Kallemeyn, 1988; Jarosewich, 1990; Baker et al., 2002). CM chondrites have experienced aqueous alteration (e.g., Krot et al., 2003). Most of the water in carbonaceous chondrites is structurally bound as hydroxyl (OH) groups within phyllosilicates (Brearley and Jones, 1998). Spectral observations have identified potential absorption features consistent with mineralogically bound OH, interlayer-molecular H_2O in phyllosilicates, and H_2O ice on some carbonaceous chondrite-like asteroids (Takir and Emery, 2012). Impacts including carbonaceous chondrite-like asteroids may involve "water" in various forms: bound-OH, interlayer H_2O, and H_2O ice. Impacts between carbonaceous chondrite-like asteroids and relatively anhydrous asteroids have probably already occurred in the Solar System.

The Dawn Spacecraft mission findings reveal exogenic carbonaceous chondrite material in the regolith of the otherwise nearly anhydrous asteroid 4 Vesta (McCord et al., 2012; De Sanctis et al., 2012; Reddy et al., 2012; Prettyman et al., 2012; Jaumann et al., 2014), the interpreted parent body for howardite meteorites (e.g., McSween et al., 2013). Howardite meteorites are polymict breccias that often contain fragments of exogenic material, most commonly material that resembles CM or CR chondrites (Wilkening, 1973; Buchanan et al., 1993; Zolensky et al., 1996; Gounelle et al., 2003; Prettyman

et al., 2012; Lunning et al., 2016). It has been argued that most of this carbonaceous chondrite material was emplaced in the vestan regolith by one relatively large impact potentially the impact that formed the Veneneia (diameter 400 ± 20 km) impact basin which partially underlies the Rheasilvia (diameter 500 ± 20 km) impact basin on Vesta's (diameter at its longest dimension = 572 km) south pole (Jaumann et al., 2012; Schenk et al., 2012; Reddy et al., 2012). The Rheasilvia or Veneneia impacts could have potentially ejected molten droplets, which could subsequently be archived in vestan regolith, and ultimately in regolithic howardite meteorites. Carbonaceous chondrite and other exogenic fragments are found in meteorite breccias that are predominately composed of material from other meteorite groups, which suggests impact mixing between separate types of asteroids is not uncommon (e.g., Rubin and Bottke, 2009).

Here, we focus on determining the provenance and petrogenesis of potential CV and CM chondrite melt clasts. Additionally, we explore how impact melting may have affected their volatile components, and intrinsic oxygen and sulfur fugacities.

2. MATERIALS AND METHODS

In the course of conducting an optical survey of all the CV chondrite thin sections in the U. S. National Meteorite Collection at the Smithsonian Institution, the principal author (NGL) recognized possible impact melts in LAR 06317 and RBT 04143. This study focused on objects that could be recognized with plane-polarized light microscopy in thin section (~30 μm thick); thus, only objects approximately larger than 30-μm were considered in this study. Smaller objects, such as some of those described by Zolensky et al. (2015), may be present in this samples, but were not sought out in this study. The similarity to the impact melts in LAR 06317 and RBT 04143 of one impact melt clast in howardite GRO 95574 was recognized during separate but concurrent research projects (Lunning et al., 2015; Lunning et al., 2016).

The Meteorite Working Group (MWG) and the Smithsonian Institution (for sections ending in ",2") allocated meteorite thin sections in this study: LAR 06317,2; LAR 06317,11; RBT 04143,2; and GRO 95574,17. LAR 06317 and RBT 04143 are CV3 chondrites (Satterwhite and Righter, 2007, 2008). The entire area of each of these thin sections (Supplementary Figs. 1–4) was examined for potential impact melt clasts. For the howardite GRO 95574, only the olivine dominated impact melt clast that mineralogically resembles the others in this study will be discussed.

2.1. Electron and scanning electron microscopy

Electron microprobe (EMP) analyses were performed with a Cameca SX-100 at the University of Tennessee, Knoxville, using wavelength-dispersive spectrometry (WDS) on thin sections. Spot analyses of olivine, high-Ca pyroxene, and chromite were conducted with a 1-μm beam, plagioclase with a 5-μm beam, and glass with a 10-μm beam, using 15 kV accelerating voltage and 30 nA beam current (or 20 kV accelerating voltage and 100 nA beam current for Mg-rich olivine and pyroxene grains). Analyses used the Pouchou and Pichoir (1984) correction model. Analyses of natural and synthetic standards were conducted daily, and 99–101% consistency with standards' known compositions was maintained. Bulk compositions of each melt clast were calculated as the unweighted average of EMP grids/lines across each clast using the glass point analysis set-up described above. All points for bulk silicate elemental compositions were collected with their centers at least 20-μm from the nearest grid point to prevent overlap between the 10-μm beam spots.

Features too small to analyze with EMP were investigated by NanoSEM analysis, using the FEI Nova NanoSEM 600 field emission scanning electron microscope fitted with a ThermoFisher energy dispersive X-ray (EDS) detector, in the Department of Mineral Sciences at the Smithsonian Institution. Maps and spot analyses were collected at a 15 kV accelerating voltage and with a beam current of 2–3 nA. Nanometer-scale data were processed with Noran System Six (NSS) software, which allows for a complete energy spectrum to be stored in each map pixel. Bulk elemental compositions of whole FeNiS globules, as well as individual minerals, were determined by extracting EDS spectra from corresponding areas, using NSS. EDS spectra were extracted to determine the chemistry of Clast mIM chromites because of their <5 μm sizes. EDS quantitative analyses were conducted using standards. EDS analyses calibrated with primary standards (FeS_2 and pure Fe metal and pure Ni metal) were used to analyze secondary standards, resultant analyses of separate secondary standards were consistently within ±2 wt.% of known composition of those secondary standards (FeS and FeNi alloys).

Mineral modal abundances for each impact melt clast were determined with ENVI 4.2 software and 8-bit gray scale backscatter electron (BSE) images. Regions of interest (ROIs) were defined based on spot analyzes for the phases (e.g., glass and olivine) present. In these ROIs, ranges of pixel values (shades of gray) were assigned to each phase based on prior mineral characterizations with petrographic, EMP, and SEM analyses. The ENVI software program displays the classification on the BSE image, which enabled the user to check the classification against the known phase occurrences of the samples (from EMP spot analyses and petrography). Cracks and holes within each clast were excluded. When present in BSE images, the host meteorite was excluded by masking. The ENVI classification for modal analyses was conducted by NGL for all the clasts in this study within a single two-day period for internal consistency. These modes are appropriate for comparing the abundances of phases between the clasts in this study. We do not use these modes beyond comparison between the different clasts.

2.2. Raman spectroscopy

The method of Zajacz et al. (2005) can be used to measure water concentrations in broad range of silicate glass compositions, including compositions from rhyolite to

basalt, from Raman spectra of glasses. To test for the presence of water, glasses within the clasts were analyzed *in situ* by Raman spectroscopy at the Vibrational Spectroscopy Laboratory at Virginia Tech. Spectra were collected using a JY Horiba LabRam HR800 Raman microprobe system with a 514 nm, 5 W argon ion laser and nitrogen-cooled CCD detector. The spectral region of interest corresponding to water in silicate glass ranges from ~3400 to 3600 cm^{-1} (Thomas, 2000; Severs et al., 2007). Detection limits for water in silicate glass are very dependent on background signal from the sample. In samples with low background, detection limits as low as 0.2 wt.% H_2O are achievable (Le Losq et al., 2012); if the background intensity is high, the detection limits are much higher and vary with background intensity (Severs et al., 2007). Our background levels were high as a result of a highly fluorescent epoxy cement that was used to make the thin sections investigated in this study. The detection limits for our analyses are estimated to be ~2 wt.% H_2O (Supplementary Figs. 5 and 6).

2.3. Oxygen three-isotope analyses

In situ oxygen three-isotope analyses were conducted on a Cameca IMS 1280, a large-radius double-focusing secondary ion mass-spectrometer (SIMS) at the WiscSIMS Lab, University of Wisconsin, Madison. Analytical conditions and data reduction are similar to those described previously (Kita et al., 2010; Tenner et al., 2013). The primary Cs^+ beam was focused to a 15 μm diameter spot with an intensity of 3 nA. Matrix effects were evaluated from olivine standards (Fo_{60}, San Carlos/Fo_{89}, and Fo_{100}) and instrumental biases of unknowns were corrected as a function of their Fo# as determined by EMP analysis. Four bracket analyses on the San Carlos olivine standard were completed before and after sets of 12 unknown analyses; most of the SIMS analyses in this session were part of a separate study of Mg-rich olivine in howardites, and the olivines analyzed outside of the clast of interest to this study (Clast mIM) have oxygen three-isotope compositions consistent with HED meteorites (Lunning et al., 2015). Typical reproducibility (spot-to-spot, in 2 standard deviation; 2SD) of the San Carlos olivine standard was ~0.3‰ for $\delta^{18}O$, $\delta^{17}O$, and $\Delta^{17}O$. Uncertainties for the San Carlos olivine standard were calculated from the 40 bracket analyses and were 0.3‰ for $\delta^{18}O$, 0.15‰ for $\delta^{17}O$, and 0.056 ‰ for $\Delta^{17}O$ (propagated 2σ standard error). Definitions of oxygen-three isotope delta-notation and the full bracket analyses data set can be found in Lunning et al. (2015).

3. RESULTS

3.1. Host meteorites

Satterwhite and Righter (2007, 2008) classified RBT 04143 and LAR 06317 as CV3 chondrites. Our petrographic work supports these classifications, and we further determined the subtypes and shock grades of these meteorites. RBT 04143 is a reduced CV3.5-3.9 chondrite ($CV3_{red}$) with a shock grade of S3. Although not exhibited in the section of RBT 04143 studied here, Ishida et al. (2012) reported evidence of brecciation in some of the thin sections included in their study. LAR 06317 is a brecciated, oxidized Allende-type CV3.5-3.9 chondrite ($CV3_{oxA}$) with a shock grade of S3. In addition, GRO 95574 is a regolithic howardite with a shock grade of at least S2 (Cartwright et al., 2014; Lunning et al., 2016). All shock grades were assigned using the shock classification scheme developed for ordinary chondrites by Stöffler et al. (1991). Petrographic descriptions associated with these expanded petrologic characterizations are detailed in the Electronic Annex.

3.2. Melt clast descriptions

In this study, we will describe five melt-derived objects; objects composed of quenched liquid (i.e. glass) and/or minerals that rapidly crystallized from a liquid. All of these objects are clast-free. None of these objects are melt-matrix breccias with unmelted clasts mixed into them when they were molten, although rare olivine microphenocrysts contain relict Mg-rich cores. We describe all of these objects as microporphyritic, meaning they are composed of microphenocrysts of olivine in groundmasses of glass or minerals that grew between the microphenocrysts (e.g., Fig. 2). For simplicity, we will refer to all five melt-derived objects collectively as "clasts" even though one is technically a melt pocket and another is a melt droplet, as will be interpreted respectively in Sections 4.2.2 and 4.2.3. We found three melt clasts in two thin sections of LAR 06317. One melt pocket occurs in RBT 04143 and one non-HED impact melt droplet was found in GRO 95574 (Fig. 1). Bulk silicate elemental compositions of the clasts are listed in Table 1, and the petrographic modes (vol.%) of their minerals and glass are listed in Table 2.

3.2.1. LAR 06317,11 Clast A

Clast A in LAR 06317,11 is ~250-μm in its longest dimension (Fig. 1a). It has a microporphyritic texture and is composed of euhedral, compositionally zoned olivine microphenocrysts (~10–50 μm) in a groundmass of translucent pink, optically isotropic glass containing accessory FeNiS globules and chromite. The glass has small (⩽10 μm) semi-spherical voids that are possibly vesicles but, in this clast, cannot definitively be distinguished from voids that formed by material plucked during polishing. Clast A is a fragmental clast in a breccia: along the contact between Clast A and the host meteorite, otherwise euhedral–subhedral olivines within Clast A are broken (Supplementary Fig. 7).

In Clast A, the olivine microphenocrysts are compositionally zoned with relatively Mg-rich cores grading to more Fe-rich rims. One olivine microphenocryst in this clast contains a relict core (Fo_{93} with molar Fe/Mn = 135) marked by an optical discontinuity. Most olivine microphenocrysts in Clast A have cores with ~Fo_{85} which zone to Fo_{63} rims (Table 3), and have molar Fe/Mn = 103–150. Glass in Clast A contains, on average, 14.1 wt.% FeO (Table 4), and has a composition that, by the CIPW norm, would primarily crystallize as plagioclase, diopside, and hypersthene. The chromite is Al-rich (hercynitic) (Supplementary Table 1).

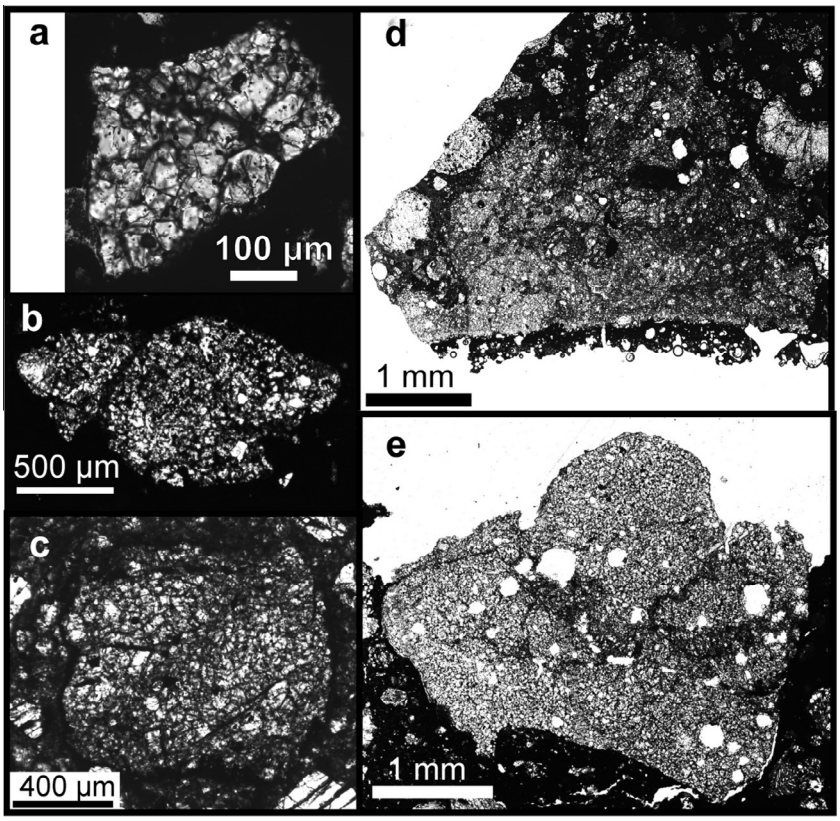

Fig. 1. Plane polarized light images of impact melt clasts. (a) Clast A in LAR 06317,11. (b) Clast C in LAR 06317,2. (c) Clast mIM in GRO 95574,17. (d) Clast Z in RBT 04143,2. (e) Clast B in LAR 06317,2.

Table 1
Average bulk silicate elemental composition of melt clasts in wt.%. EMP 3σ errors propagated for elemental ratios listed in paratheses.

	LAR 06317,11 Clast A	LAR 06317,2 Clast B	LAR 06317,2 Clast C	RBT 04143,2 Clast Z	GRO 95574,17 Clast mIM
n	116	192	213	149	229
P_2O_5	0.28	0.88	0.24	0.15	0.27
SiO_2	39.6	37.7	37.7	43.4	43.7
SO_2	0.18	0.15	0.24	0.33	0.59
TiO_2	0.17	0.10	0.15	0.21	0.22
Al_2O_3	3.77	3.54	3.33	5.40	4.84
Cr_2O_3	0.27	0.45	0.57	0.59	0.55
MgO	28.6	28.7	29.2	29.7	21.3
CaO	3.05	2.42	2.55	3.76	4.02
MnO	0.19	0.19	0.19	0.22	0.36
FeO	23.5	26.2	25.9	15.8	23.4
Na_2O	0.58	0.48	0.53	0.65	0.85
K_2O	0.05	0.04	0.04	0.05	0.07
Total	100.3	100.3	100.5	100.3	99.9
wt.% ratios					
Mg/Si	1.09 (0.022)	1.15 (0.023)	1.17 (0.024)	1.03 (0.021)	0.73 (0.015)
Al/Si	0.126 (0.003)	0.124 (0.003)	0.117 (0.003)	0.165 (0.004)	0.146 (0.003)
Ca/Si	0.115 (0.004)	0.096 (0.004)	0.102 (0.004)	0.130 (0.004)	0.138 (0.004)
Ca/Al	0.915 (0.040)	0.776 (0.040)	0.869 (0.044)	0.789 (0.026)	0.941 (0.031)
Na/Ca	0.235 (0.042)	0.240 (0.056)	0.252 (0.054)	0.212 (0.036)	0.259 (0.035)
Mn/Al	0.073 (0.045)	0.078 (0.049)	0.085 (0.055)	0.059 (0.028)	0.109 (0.039)

Table 2
Mineral percentages for each melt clast.

	LAR 06317,11 Clast A	LAR 06317,2 Clast B	LAR 06317,2 Clast C	RBT 04143,2 Clast Z	GRO 95574,17 Clast mIM
Olivine	72	87	76	60	62
Glass	27		20	38	37
Chromite	0.8	2.0	2.2		
FeNiS globules	0.5	1.4	1.9	1.7	1.1
Plagioclase		6.7			
High-Ca pyroxene		2.6			
Silicate re-normalized modes					
Olivine	73	90	80	61	63
Glass	27		20	39	37
Plagioclase		7			
High-Ca pyroxene		3			

FeNiS globules in Clast A have circular shapes (two-dimensionally) and are ~10 μm in diameter (Fig. 3a). These globules have bulk elemental compositions with 1–3 wt.% Ni (Table 5). They contain at least two phases: FeNi-metal and pyrrhotite monosulfide solid solution (MSS). The FeNiS globules by volume are predominantly pyrrhotite MSS (85–90%), while the FeNi-metal is sub-μm-sized and is ~11 wt.% Ni.

3.2.2. LAR 06317,2 Clast B

Clast B in LAR 06317,2 is ~3.5 mm in its longest dimension (Fig. 1e). It has a microporphyritic texture and is composed of compositionally zoned subhedral olivine microphenocrysts (~10–150 μm) in a groundmass of anisotropic plagioclase and high-Ca pyroxene with accessory FeNiS globules (Fig. 3b and c) and chromite. The growth of the groundmass minerals was constrained between the larger olivine microphenocrysts; for instance, laths of plagioclase stretch from one olivine microphenocryst to another. Clast B contains vesicles with circular cross sections (40–100 μm across), surrounded by groundmass composed of crystals that are small (~10–20 μm) compared to the vesicles. Unlike in Clast A, the groundmass crystals in Clast B are generally unbroken along the menisci of the vesicles, and several vesicles are lined with translucent orange-brown glass. Clast B is a fragmental clast in a breccia: along the contact between Clast B and the host meteorite, otherwise euhedral mineral grains within Clast B are incomplete and broken on the edge (Supplementary Fig. 8).

Olivine microphenocrysts in Clast B are compositionally zoned from relatively Mg-rich cores to more Fe-rich rims. Most olivine microphenocrysts in Clast B have ~ Fo_{85} cores that progressively transition to rims as Fe-rich as Fo_{58} (Table 3); these olivines have molar Fe/Mn = 84–187. Rare olivine microphenocrysts in this clast contain very Mg-rich cores (Fo_{97-99}) with Fe/Mn = 13–47, grading into compositions more typical of olivine in this clast. The chromite is Al-rich (Supplementary Table 1). The plagioclase is relatively high-Ca (~$An_{75}Ab_{25}$) and is notably Fe-rich, with 1.1 wt.% FeO (Supplementary Table 2). In plane-polarized light, plagioclase grains do not exhibit discoloration indicative of terrestrial weathering redistribution of Fe, however, this possibility cannot be definitively ruled out. The high-Ca pyroxene in Clast B is relatively high-Al (Supplementary Table 3: 8–11 wt.% Al_2O_3), and thus cannot be properly represented on the pyroxene quadrilateral (En-Fs-Wo). This clast contains <1% quenched mesostasis as <5 μm-sized areas that vary in composition but consistently contain Fe, Ca, P, and Si.

FeNiS grains in Clast B are groundmass components along with plagioclase and high-Ca pyroxene (Fig. 3b and c). These opaque grains range from 1 to 50 μm in size. Fig. 3c illustrates a region where FeNiS grains are almost solely composed of a single phase, usually pyrrhotite MSS. Additionally, Clast B contains a few two-phase FeNiS globules composed of pyrrhotite MSS-pentlandite or pyrrhotite MSS-FeNi-metal. The pentlandite in the two-phase opaque grains has ~19 wt.% Ni, ~44 wt.% Fe, and ~35 wt.% S. The two-component FeNiS grains have bulk Ni concentrations that range from 0 to 3 wt.% Ni (Table 5). These multi-phase grains are rare compared to single-phase pyrrhotite MSS grains, while the other two phases occur in the groundmass and have irregular shapes.

3.2.3. LAR 06317,2 Clast C

Clast C in LAR 06317,2 is ~1.5-mm in its longest dimension (Fig. 1b). It has a microporphyritic texture and is composed of compositionally zoned, subhedral–euhedral olivine grains (~10–200 μm) in a mostly glassy groundmass with accessory FeNiS globules and chromite (Fig. 3d and e). The groundmass glass in Clast C is optically isotropic and contains delicate vitrophyric phases (≪1 μm across in narrowest direction). Clast C may contain vesicles but their features are not as diagnostic as those in Clast B: these voids have smoothly curved, glass-lined edges in cross section. A few isolated regions of the groundmass appear to contain laths of plagioclase, but these laths (1–3 μm across) are too thin for anisotropy to be petrographically assessed. Along the contact between Clast C and its host meteorite, olivine grains within Clast C are broken (Supplementary Fig. 9).

The olivine microphenocrysts in Clast C typically have Mg-rich cores (~Fo_{85}) that zone to rim compositions as Fe-rich as Fo_{50}, with molar Fe/Mn ratios of 83–184. Several olivine microphenocrysts have cores that are more Mg-rich (Fo_{97-99}) with Fe/Mn = 12–21, grading into the olivine compositions more typical of this clast. The glass

Table 3
Representative olivine analyses. Below detection limit values denoted by b.d.

	LAR 06317,11 Clast A			LAR 06317,2 Clast B			LAR 06317,2 Clast C			RBT 04143,2 Clast Z			GRO 95574,17 Clast mIM		
	Relict core*	Core	Rim	Relict core	Core	Rim	Relict core	Core	Rim	Relict core	Core	Rim	Relict core	Core	Rim
P_2O_5	b.d.	0.05	0.04	b.d.	0.17	0.04	b.d.	0.06	0.04	b.d.	0.05	0.03	0.03	0.17	0.15
SiO_2	41.6	39.4	36.1	41.8	38.5	35.4	41.7	39.1	34.5	42.5	39.8	37.3	42.0	39.6	37.7
TiO_2	0.04	0.02	b.d.	0.11	b.d.	0.02	0.06	0.02	b.d.	0.03	b.d.	0.02	0.01	b.d.	0.03
Al_2O_3	0.04	0.06	0.07	0.11	0.15	0.08	0.11	0.09	0.07	0.03	0.07	0.89	0.07	0.06	0.08
Cr_2O_3	0.05	0.28	0.22	0.25	0.32	0.22	0.30	0.29	0.10	0.51	0.41	1.01	0.54	0.34	0.52
MgO	51.5	43.7	30.1	54.3	44.4	27.5	55.8	44.8	24.0	56.0	46.2	38.0	54.6	45.7	37.4
CaO	0.35	0.16	0.24	0.34	0.23	0.48	0.32	0.20	0.69	0.23	0.28	0.32	0.21	0.17	0.22
MnO	0.06	0.13	0.23	0.19	0.14	0.27	0.08	0.11	0.30	0.14	0.14	0.21	0.19	0.18	0.31
FeO	6.68	16.1	32.2	2.57	15.8	35.2	1.30	15.6	40.6	1.07	12.9	21.8	2.90	14.4	24.2
NiO	0.03	0.07	0.12	b.d.	0.04	0.04	b.d.	0.11	0.02	b.d.	0.21	0.11	0.02	0.08	0.08
Total	100.3	99.9	99.3	99.7	99.8	99.2	99.6	100.4	100.4	100.5	100.2	99.7	100.5	100.7	100.7
P	b.d.	0.001	0.001	b.d.	0.004	0.001	b.d.	0.001	0.001	b.d.	0.001	0.001	0.001	0.003	0.003
Si	1.001	0.995	0.996	0.995	0.976	0.995	0.989	0.983	0.985	0.998	0.991	0.977	0.993	0.987	0.985
Ti	0.001	b.d.	b.d.	0.002	b.d.	0.0	0.001	0	b.d.	0.001	b.d.	0	0	b.d.	0
Al	0.001	0.002	0.002	0.003	0.004	0.003	0.003	0.003	0.002	0.001	0.002	0.027	0.002	0.002	0.002
Cr	0.001	0.006	0.005	0.005	0.006	0.005	0.006	0.006	0.002	0.009	0.008	0.021	0.01	0.007	0.011
Mg	1.849	1.646	1.237	1.93	1.676	1.149	1.972	1.68	1.023	1.958	1.716	1.48	1.928	1.694	1.458
Ca	0.009	0.004	0.007	0.009	0.006	0.014	0.008	0.005	0.021	0.006	0.007	0.009	0.005	0.005	0.006
Mn	0.001	0.003	0.005	0.004	0.003	0.006	0.002	0.002	0.007	0.003	0.003	0.005	0.004	0.004	0.007
Fe	0.135	0.34	0.742	0.051	0.335	0.826	0.026	0.328	0.969	0.021	0.269	0.476	0.057	0.301	0.529
Ni	0	0.002	0.003	0	0.001	0.001	0	0.002	0	0	0.004	0.002	0	0.002	0.002
Total	2.998	2.999	2.999	2.999	3.013	3.000	3.006	3.011	3.011	2.996	3.002	2.998	3	3.004	3.003
Fo	93.2	82.9	62.5	97.4	83.3	58.2	98.7	83.7	51.4	98.9	86.4	75.7	97.1	84.9	73.4
Fe/Mn	135	113	148	13	111	138	13	164	138	7	89	95	14	75	75

* Relict core in Clast A is defined by an optical discontinuity.

Table 4
Average glass compositions.

	LAR 06317,11 Clast A		LAR 06317,2 Clast C		RBT 04143,2 Clast Z		GRO 95574,17 Clast mIM	
n	14		15		10		9	
	Average	1σ S.D.	Average	1σ S.D.	Average	1σ S.D.	Average	1σ S.D.
P_2O_5	1.05	0.07	1.24	0.05	0.29	0.08	0.49	0.03
SiO_2	48.0	0.3	42.0	0.3	49.9	3.5	49.4	0.8
SO_2	0.36	0.11	0.69	0.10	0.43	0.26	0.85	0.13
TiO_2	0.79	0.03	0.82	0.05	0.50	0.14	0.42	0.05
Al_2O_3	16.5	0.4	16.7	0.5	12.0	3.1	9.4	0.5
Cr_2O_3	0.08	0.01	0.03	0.02	0.43	0.15	0.23	0.05
MgO	1.56	0.08	1.46	0.30	8.90	7.87	4.22	0.87
CaO	14.1	0.1	15.0	0.8	9.2	2.8	7.7	0.5
MnO	0.16	0.02	0.16	0.02	0.27	0.03	0.44	0.02
FeO	14.1	0.5	18.6	1.4	15.9	3.1	24.7	0.9
Na_2O	2.47	0.08	3.00	0.43	1.49	0.23	1.77	0.13
K_2O	0.17	0.02	0.20	0.03	0.11	0.41	0.14	0.04
Total	99.4	0.3	99.5	0.6	99.4	1.1	99.8	0.4
P	0.13	0.01	0.16	0.01	0.04	0.01	0.06	0.00
Si	7.15	0.03	6.54	0.02	7.39	0.41	7.58	0.07
S	0.05	0.02	0.10	0.01	0.06	0.04	0.12	0.02
Ti	0.09	0.00	0.10	0.01	0.06	0.01	0.05	0.01
Al	2.89	0.05	3.06	0.08	2.09	0.52	1.70	0.08
Cr	0.01	0.00	0.00	0.00	0.05	0.02	0.03	0.01
Mg	0.35	0.02	0.34	0.07	1.98	1.77	0.97	0.21
Ca	2.25	0.02	2.51	0.13	1.45	0.43	1.26	0.07
Mn	0.02	0.00	0.02	0.00	0.03	0.00	0.06	0.00
Fe	1.76	0.07	2.42	0.19	1.98	0.42	3.17	0.14
Na	0.71	0.02	0.91	0.12	0.43	0.11	0.53	0.04
K	0.03	0.00	0.04	0.01	0.02	0.01	0.03	0.01
Total	15.44	0.04	16.21	0.07	15.57	0.64	15.56	0.09
H_2O	b.d.		b.d.		b.d.		b.d.	

Table 5
Bulk Composition of FeNiS Globules in wt.%.

	LAR 06317,11 Clast A		LAR 06317,2 Clast B			LAR 06317,2 Clast C			RBT 04143,2 ClastZ	GRO 95574,17 Clast mIM
	Globule1	Globule2	Globule1	Globule2	Globule3	Globule1	Globule2	Globule3	Globule1	Globule1
S	32	31	35	36	37	31	32	32	18	32
Fe	64	64	62	60	63	61	61	60	75	58
Ni	1	3	0	5	0	5	3	6	7	10
Total	97	97	97	98	99	97	97	97	100	101

in Clast C has an average composition that is 18.6 wt.% FeO (Table 4) and has a CIPW normative composition that would primarily crystallize plagioclase, nepheline, diopside, and olivine. Clast C's chromite is Al-rich (Supplementary Table 1). The plagioclase is relatively high-Ca ($\sim An_{72}Ab_{28}$) and relatively Fe-rich, with 1.6 wt.% FeO (Supplementary Table 2). We looked for but did not observe any orange-rusty-discoloration associated with this plagioclase that would indicate this Fe was redistributed into the plagioclase by terrestrial weathering.

In Clast C, FeNiS globules are irregularly-shaped with smoothly curved edges and are 10–20 μm in size (Fig. 3d and e). These globules have bulk elemental compositions with 3–6 wt.% Ni (Table 5). They consistently contain two phases, FeNi-metal and pyrrhotite MSS, and sometimes contain a high-Ni sulfide as a third phase. These FeNiS globules by volume are predominantly pyrrhotite MSS (80–94%). The FeNi metal and high-Ni sulfides are typically μm- to sub-μm-scale in size. Stoichiometric pentlandite occurs as <1% to 14% of the globule volume—this high-Ni sulfide has a mineral chemistry of ~21 wt.% Ni, ~41 wt.% Fe, and ~33 wt.% S. The FeNi-metal is consistently ~5% of the globule volume, μm-sized, and has a composition of ~43 wt.% Ni.

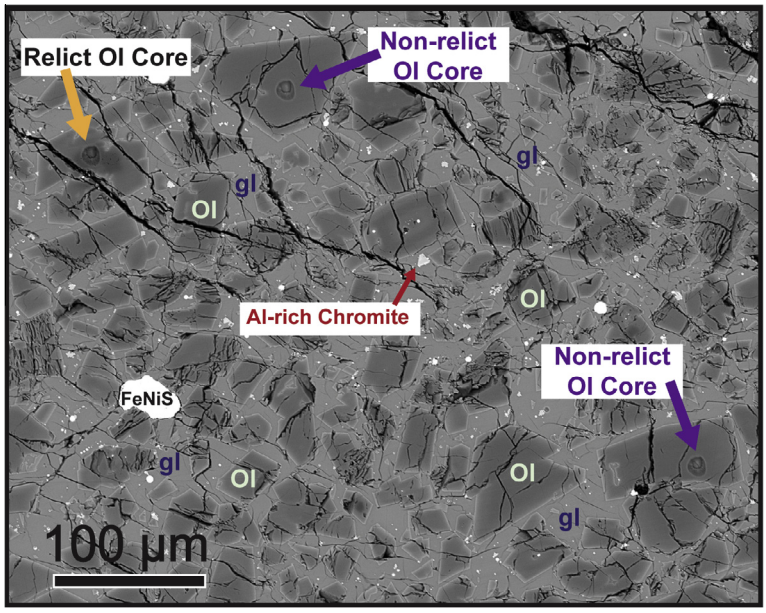

Fig. 2. Backscatter electron (BSE) image texture of Clast mIM in GRO 95574,17. The texture of this clast is generally representative of the textures of clasts in this study. Zoned equant microphenocrysts of olivine with Mg-rich (medium gray) cores and more Fe-rich (lighter medium gray) rims. Representative olivine microphenocrysts labeled 'Ol' and pools of glass labeled with 'gl.' Accessory intergranular zoned chromite (light gray) and FeNiS globules (white). This image SIMS spots from oxygen three-isotope analyses are visible and labeled with arrows.

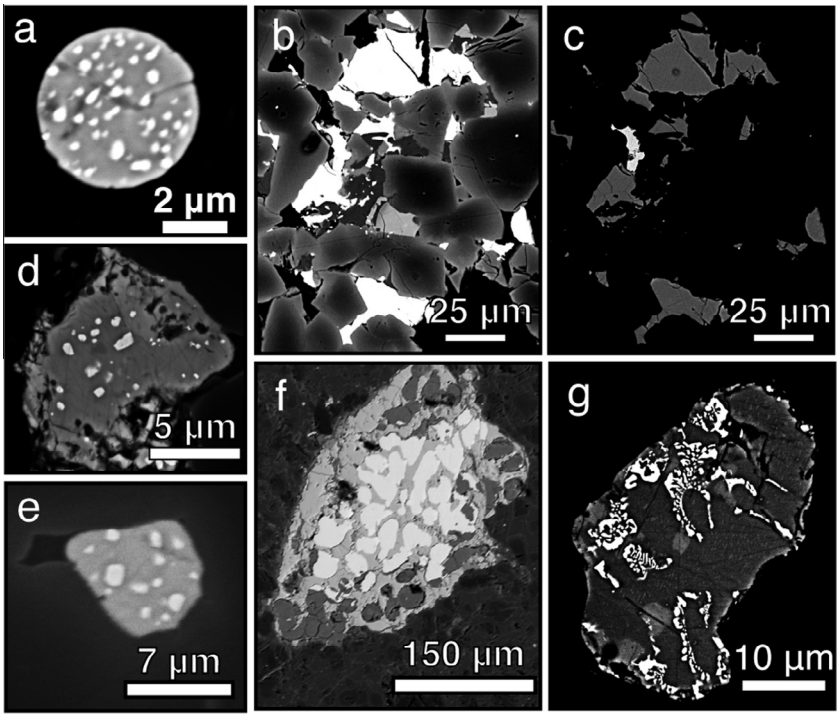

Fig. 3. Backscatter electron (BSE) images of FeNiS globules or grains in (a) Clast A in LAR 06317,11; white corresponds to the FeNi metal and medium gray is pyrrhotite monosulfide solid solution (MSS). (b) Clast B in LAR 06317,2; white corresponds to the metal and sulfide grains. (c) Same field of view of Clast B in LAR 06317,2; white corresponds to the FeNi metal and medium gray is pyrrhotite MSS. (d) Clast B in LAR 06317,2; white corresponds to the FeNi metal, dark gray is pyrrhotite MSS, and medium-lighter gray is Ni-rich sulfide. (e) Clast B in LAR 06317,2; white corresponds to the FeNi metal, light gray is pyrrhotite MSS, and dark grays are surrounding zoned olivines. (f) Clast Z in RBT 04143,2; white corresponds to the FeNi metal, dark gray is pyrrhotite MSS, and medium-lighter gray in the globule is Fe-oxides that likely formed from terrestrial weathering. (g) Clast mIM in GRO 95574,14; white corresponds to the FeNi metal, dark gray is pyrrhotite MSS, and medium-lighter gray is pentlandite.

3.2.4. RBT 04143,2 Clast Z

Clast Z in RBT 04143,2 is ~4 mm in its longest dimension (Fig. 1d). It has a microporphyritic texture and is composed of compositionally zoned, subhedral–euhedral olivine microphenocrysts (~5–100 μm) and FeNiS globules in a glassy groundmass (Figs. 2 and 3e and f). The groundmass glass in Clast Z contains delicate vitrophyric phases (≪1 μm across in their narrowest direction); this glass is translucent with an orange-brown hue. Clast Z contains vesicles, which have smooth curved edges in cross section and the menisci along their edges are apparent in plane-polarized light when the focal point is raised/lowered. Clast Z interfingers with the host material. There are no fragmental/broken olivine microphenocrysts along the boundary between Clast Z and its host meteorite (Supplementary Figs. 10 and 11).

The olivine microphenocrysts in Clast Z typically have Mg-rich cores (~Fo_{85}) which transition to rims as Fe-rich as Fo_{71} with molar Fe/Mn = 62–197. Rare olivine microphenocrysts have more Mg-rich cores ($Fo_{97–99}$) with Fe/Mn = 7–32, grading into the typical olivine compositions in this clast. The glass in Clast Z has an average FeO concentration of 15.91 wt.% (Table 4), and its CIPW norm composition would primarily crystallize plagioclase, diopside and hypersthene. Unlike the other melt clasts in this study, we did not find any chromite in Clast Z.

Clast Z contains two large (200–300-μm) FeNiS globules and small, finely disseminated μm-scale FeNiS globules. The relatively large globules have cellular textures with circular grains of metal surrounded by sulfide (Fig. 3f). The sulfide is consistently the troilite end member (62 wt.% Fe and 38 wt.% S) of the pyrrhotite MSS. Some of the metal grains have been altered to FeNi-oxides that are bright orange-red in plane-polarized light. Given that its host meteorite (RBT 04143) is an Antarctic find, we surmise that this alteration is due to terrestrial weathering. In the large FeNiS globule with fewer altered metal grains (Fig. 3f), the globule is 48% troilite and 52% metal by volume. If we added the FeNi-oxides that follow the cellular texture (which likely replaced primary FeNi-metal), the percentage of metal would be even higher. The metal grains are zoned with regard to Ni-concentration; the metal is predominately 9 wt.% Ni (EMP analyses), but along their edges of some metal grains the Ni-concentration reaches 31 wt.% Ni (EMP analyses). The spacing between metal grains in Clast Z's FeNiS globule is larger than in any of the other melt clasts in this study (Fig. 3), and indicates that this globule records the minimum cooling rate for the melt clasts in this study: ~16 °C/s calculated from spacing of FeNi-metal cells within troilite (both within FeNiS globules) using the method of Scott (1982). The errors for cooling rates calculated from FeNi-metal-troilite cell/dendrite spacing without other constraints are estimated to be a factor of 3–5 times the calculated value (Scott, 1982).

3.2.5. GRO 95574,17 Clast mIM

Clast mIM in the howardite GRO 95574,14 is ~1 mm across and is roughly equidimensional (Fig. 1c). It contains compositionally zoned olivine microphenocrysts (5–100 μm) in a groundmass of optically isotropic glass with accessory FeNiS globules and sub-μm-scale chromite (Figs. 2 and 3g). Along the boundary between the clast and its host meteorite, most of the olivine microphenocrysts in Clast mIM are aligned and/or unbroken, and some stretches along its edge are marked by μm-wide sulfide ribbons (opaque in Fig. 1c). Although most of the olivine grains along the boundary between Clast mIM and its host are unbroken, there are some exceptions (Supplementary Figs. 12 and 13).

The olivine microphenocrysts typically have Mg-rich cores with ~Fo_{85}, which zone to rim compositions as Fe-rich as Fo_{73}: these olivines have molar Fe/Mn = 64–126. A few olivine microphenocrysts have more Mg-rich cores ($Fo_{97–99}$) with Fe/Mn = 14–17, grading into the more typical olivine compositions. The oxygen three-isotope signature of a very Mg-rich relict olivine core (Fo_{99} with Fe/Mn = 14) is $\delta^{18}O = -5.7 \pm 0.4‰$, $\delta^{17}O = -9.0 \pm 0.4‰$ and $\Delta^{17}O = -6.0 \pm 0.4‰$ (errors are 2σ SD). Additionally, we measured the oxygen three-isotope signatures of two more typical Mg-rich olivine cores (errors are 2σ SD): One olivine core (Fo_{86}) has $\delta^{18}O = 5.5 \pm 0.4‰$, $\delta^{17}O = 0.2 \pm 0.4‰$ and $\Delta^{17}O = -2.6 \pm 0.4‰$ and another typical olivine core (Fo_{86}) has $\delta^{18}O = 6.3 \pm 0.4‰$, $\delta^{17}O = 0.2 \pm 0.4‰$ and $\Delta^{17}O = -3.1 \pm 0.4‰$ (Figs. 2 and 4).

The glass in Clast mIM has an average composition of 24.7 wt.% FeO (Table 4), and Raman spectroscopy show no H_2O above the 2 wt.% detection limit (Table 4). Clast mIM's groundmass glass has a composition that, by the CIPW norm, would primarily crystallize plagioclase,

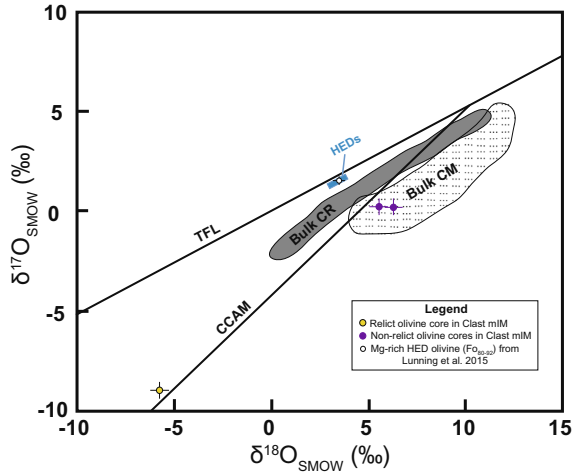

Fig. 4. Oxygen three-isotope plot of olivine in Clast mIM in the regolithic howardite GRO 95574,17. The bulk HED field includes the eucrite fractionation line and bulk HED analyses, representing Vesta. TFL refers to the terrestrial fractionation line. CCAM refers to the carbonaceous chondrite anhydrous mineral line. Bulk CR and Bulk CM fields refer to bulk analyses of CR chondrites and CM chondrites, respectively. Oxygen three-isotope compositions of meteorite groups are from Krot et al. (2003) and references therein. Known achondrites groups plot close to the HEDs or on the TFL (lunar rocks) or above the TFL (martian rocks). The oxygen three-isotope signatures of GRO 95 olivine plotted with other achondrites can be found in Lunning et al. (2015) and its Supplementary material.

diopside and hypersthene. The chromite is too small to be measured by EMP, but a quantitative EDS analysis using the NanoSEM is less Al-rich than the chromite found in the LAR 06317 melt clasts (Supplementary Table 1).

Clast mIM contains one large FeNiS globule (~30 μm) and many finely disseminated, μm-scale FeNiS globules (1–5 μm). The large globule contains FeNi metal and two sulfide phases (Fig. 3g). The most volumetrically abundant sulfide (76%) is pyrrhotite MSS, and the less abundant sulfide (15%) is Ni-rich stoichiometric pentlandite (~25 wt.% Ni, ~42 wt.% Fe, and ~35 wt.% S). The FeNi metal grains are μm- to sub-μm-scale in their narrowest dimensions, have skeletal textures, and are ~52 wt.% Ni (stoichiometry consistent with tetrataenite).

4. DISCUSSION

4.1. Melt clast provenances

Along with other features of the individual clasts described in Section 3, the major-element zoning of euhedral–subhedral olivine microphenocrysts which dominate the mineralogy of all of these clasts indicates that they rapidly crystallized under disequilibrium conditions following near-complete melting of their precursors (e.g., Lofgren, 1989; Radomsky and Hewins, 1990; Yu et al., 1995). The potential origin of these clasts can be evaluated by first considering the two fundamental rock types known to exist in the Solar System: achondrites and chondrites (Krot et al., 2003). Achondrites by definition formed on parent bodies that experienced melting, as a *primary process* that drove their differentiation. Chondrites are composed of material from the Solar System's protoplanetary disk, and some of these components experienced melting and disequilibrium crystallization prior to assembly of their parent bodies (e.g., Krot et al., 2003). However, the only known components of chondrites that resemble the clasts in this study—in texture and mineral chemistry—are the Type II (FeO-rich) Porphyritic Olivine (PO) chondrules (e.g., Johnson and Prinz, 1991; Scott and Krot, 2003; Connolly and Desch, 2004). Only one *secondary process* known to occur on both chondritic or achondritic parent bodies produces melting followed by rapid disequilibrium crystallization: shock from impacts (e.g., Scott and Krot, 2003; Bischoff et al., 2006). Thus, there are three potential origins for the melt clasts: (1) PO chondrules or PO chondrule fragments, (2) achondritic lithic clasts, or (3) impact melts. Clast Z interfingers with unmelted material from its host meteorite a CV3 chondrite, indicating melting *in situ* technically meaning it is a melt pocket rather than a fragmental clast (Supplementary Figs. 10 and 11), which is inconsistent with Clast Z potentially being a chondrule, chondrule fragment, or achondritic fragment. However, as the other four melt clasts do not exhibit textural evidence for melting *in situ*, all three possible origins need to be explored for them.

4.1.1. Evidence against an origin as chondrules or chondrule fragments

Chondrites commonly contain not only intact chondrules, but also fragments of chondrules that may have broken prior to parent body accretion (Brearley and Jones, 1998). Most of the clasts in this study texturally resemble porphyritic olivine (PO) chondrule fragments, which are composed of equant microporphyritic Fe–Mg-zoned olivine and chromite in glassy groundmasses. The olivine compositions in clasts described in this study resemble the more Fe-rich Type II (e.g. olivine Fo < 90) PO chondrules (McSween, 1977; Hewins, 1997). However, the compositions of glass and chromite in these clasts are distinct from those in Type II PO chondrules in CV chondrites. Glasses in clasts A, C, Z, and mIM are relatively Fe-rich (plagioclase and pyroxene normative) compared to the glass in Type II chondrules, which is typically feldspathic (Brearley and Jones, 1998). Chromites in Clasts A, B, and C extend to more Al-rich compositions than chromites found in Type II chondrules (Johnson and Prinz, 1991). Additionally, Clasts B and Z would be large for chondrule fragments (~3.5 mm and 4 mm across, respectively). CV chondrites have chondrules that are typically among the largest across chondrite groups; unbroken CV chondrules have reported mean diameters of 655–1000 μm (Grossman et al., 1988; Teitler et al., 2010; Friedrich et al., 2015). However, as rare components, some very large chondrules (⩾4 mm) have been described in a range of chondrite groups (Ruzicka et al., 1998; Friedrich et al., 2015).

4.1.2. Evidence against an origin as achondrite fragments

Clasts A, B, and C are found in a CV3 chondrite and accordingly it is clear that we must consider the possibility that they originated in distinct achondritic protoliths, as explained in Section 4. An achondritic precursor must also be considered for Clast mIM based on the fact that its host meteorite is an HED polymict (achondrite) breccia. As shown in Section 3.2.5, clast mIM has an oxygen isotope signature that distinguishes it from the rest of HED meteorites and hence from its host.

Achondrites with olivine chemistries and modes that are most similar to the five clasts in this study are the groups collectively known as the primitive achondrites, particularly the FeO- and olivine-rich ungrouped achondrites (e.g., LEW 88763) and brachinites (e.g., Day et al., 2012; Gardner-Vandy et al., 2012). Bulk elemental compositions cannot be used to distinguish between primitive achondrites and chondritic impact melts, because primitive achondrites have undergone only low degrees of partial melting and thus their bulk elemental compositions are very close to bulk elemental chondritic compositions. However, primitive chondrites typically have comparatively coarse-grained granoblastic textures and contain minerals that are chemically equilibrated (i.e. not zoned) with respect to their major-element chemistry (Mittlefehldt et al., 1998). In contrast, the clasts in this study have undergone near complete melting, with only very Mg-rich relict olivine ($Fo_{97–99}$) remaining unmelted. After melting, these clasts experienced rapid cooling, as evidenced by the Mg–Fe zoning in their olivine microphenocrysts, the presence of quenched vitrophyric phases, and cooling rates of roughly 16 °C/s based the spacing of the cellular metal in their FeNiS globules.

4.1.3. Evidence supporting an impact melt origin

As mentioned in Section 1, impact melting is primarily a bulk melting process when the target is a chondrite; however, in achondrites partial impact melting has been documented (e.g., Beck et al., 2012). Disequilibrium partial melting experiments have been conducted on ordinary chondrite samples (Feldstein et al., 2001). In these studies, the unmelted (restite) minerals were more Mg-rich, anhedral, and typically at least an order of magnitude larger than the microlites/microphenocrysts that grew from the partial melts (melt-grown). The microporphyritic texture of the impact melts in this study (Figs. 2 and 5) resembles the texture of the melt-grown microlites/microphenocryst and associated melt rather than restites.

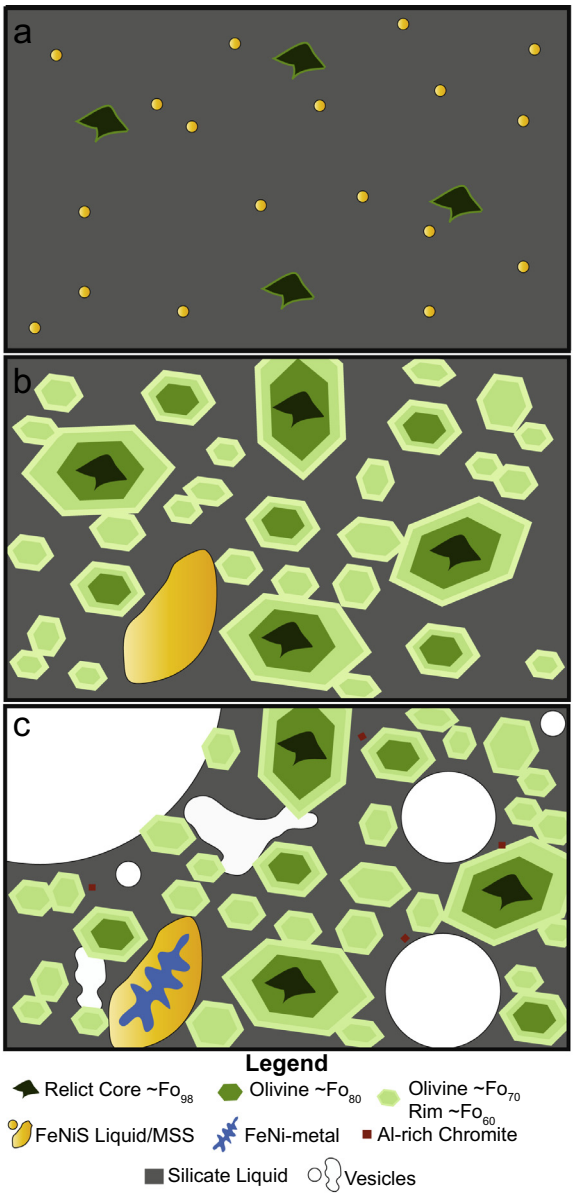

Fig. 5. Generalized impact melt formation scenario. (a) Impact induced near complete bulk melting, only very Mg-rich relict olivine are not melted. Immiscible silicate and FeNiS liquids are formed. (b) Olivine rapidly crystallizes from the silicate liquid and FeNiS liquid globules likely coalesce into larger globules. (c) Olivine continues to crystallize. If present, Al-rich chromite begins to crystallize. All of the clasts except Clast C in LAR 06317, were arrested around this point thus quenching the silicate liquid into glass and trapping vesicles (if present). Images of the slight variations on the texture illustrated here for the clasts in this study are available in Fig. 2 and Supplementary Figs. 7–13.

The five clasts in this study contain zoned olivine microphenocrysts in glass, which is a texture that resembles those of some impact melt clasts found in non-carbonaceous chondrites (e.g., Bogard et al., 1995; Bischoff et al., 2006; Metzler et al., 2011). Notably, as described in the Electronic Annex, in the host CV3 chondrites olivines in chondrules and matrix fragments are unzoned with regard to major-element chemistry, but separate olivine grains do not have the same major element composition (i.e. these are unequilibrated chondrites). Additionally, olivines in all five melt clasts do not show the shock features (e.g., undulatory extinction and/or planar fractures in host meteorites, as described in the Electronic Annex). These differences between the melt clasts and their host meteorites indicate the melt clasts have not experienced the shock or thermal metamorphism exhibited in their host meteorites.

4.2. Impact melt clasts: formation histories and precursors

In the following subsections, we consider potential precursors for each of the melt clasts using element ratios from the bulk elemental composition of each clast. We evaluate silicate bulk composition by examining ratios between lithophile elements because they should not be affected by FeNiS immiscibility. Other lines of evidence specific to the clast/host meteorite provide additional context for how each impact melt clast formed.

4.2.1. $CV3_{oxA}$ source and formation of impact melt clasts in LAR 06317

The three melt clasts in LAR 06317 have similar major-element silicate bulk compositions. Clasts A, B, and C, respectively, have wt.% ratios of Al/Si = 0.126 ± 0.003, 0.124 ± 0.003, and 0.117 ± 0.003 Ca/Si = 0.115 ± 0.004, 0.096 ± 0.004, and 0.102 ± 0.004; Na/Ca = 0.235 ± 0.042, 0.240 ± 0.056, and 0.252 ± 0.054 and Mn/Al = 0.073 ± 0.045, 0.078 ± 0.049, and 0.085 ± 0.055 (Table 1). The similarities of these ratios support the interpretation that these clasts were produced from the same precursor. Their relatively high Al/Si and Ca/Si ratios, combined with relatively low Na/Ca ratios, are consistent with the bulk elemental ratios of carbonaceous chondrites, and are notably similar to CV chondrites (Table 6). Thus, the bulk elemental compositions of the clasts are generally consistent with their forming from a CV chondrite precursor, such as their host meteorite, a $CV3_{oxA}$ chondrite.

The observation that the boundaries of the LAR 06317 clasts are fragmental provides evidence that they were once parts of larger impact melts, which were later comminuted after they solidified. Of the three fragmental impact melt clasts found in LAR 06317, Clast A appears to have been quenched earliest in its crystallization sequence, as its groundmass glass is more abundant (Table 2) and does

Table 6
Chondrite bulk composition elemental ratios.

wt.% ratio	CV	CM	CO	CR	CI	LL	L	H
Mg/Si	0.92–1.09	0.881–1.058	0.912–1.23	n/a	0.924–1.22	0.810–1.11	0.805–1.13	0.810–1.20
Al/Si	0.112–0.130	0.092–0.143	0.090–0.124	n/a	0.082–0.099	0.063–0.080	0.053–0.085	0.063–0.092
Ca/Si	0.114–0.121	0.065–0.104	0.065–0.096	0.064–0.486	0.088–0.090	0.064–0.083	0.062–0.086	0.062–0.083
Na/Ca	0.116–0.245	0.150–0.461	0.079–0.423	n/a	0.533–0.683	0.238–0.710	0.317–0.757	0.262–0.729
Mn/Al	0.081–0.088	0.102–0.194	0.095–0.124	0.998–2.10	0.181–0.221	0.184–0.276	0.163–0.300	0.167–0.308

Sources: Jarosewich (1990), Wasson and Kallemeyn (1988) and Kallemeyn et al. (1994) (no Si reported for CR chondrites).

not contain vitrophyric phases. According to the CIPW norm had it not quenched, the glass in Clast A would crystallize additional olivine (plus diopside and plagioclase). In contrast to the glasses found in Clasts A and C, Clast B crystallized not only olivine and chromite but also Al- and Ti-rich, high-Ca pyroxene ($En_{20–29}$ $Wo_{52–56}$) and plagioclase ($An_{36–59}$). The vitrophyric phases in the glass of Clast C and the overall lower fraction of glass in Clast C relative to Clast A indicate that Clast C was quenched at a later stage than Clast A (Table 2).

4.2.2. CV_{red} source and formation of Clast Z in RBT 04143

As noted in Section 4.1, the boundary between Clast Z and its host meteorite RBT 04143 interfingers with the host material (Supplementary Figs. 10 and 11). Additionally, the olivine grains are unbroken euhedral–subhedral crystals (i.e., there are no fragmental grains) along the boundary between Clast Z and the surrounding meteorite. This contact indicates that this clast is a melt pocket, which melted *in situ* from material of its host meteorite, a $CV3_{red}$ chondrite. Additionally, the bulk silicate elemental composition of Clast Z—relatively high Al/Si and Ca/Si ratios combined with relatively low Na/Ca and Mn/Al ratios (Tables 1 and 6)—is consistent with its formation from a CV chondrite precursor.

4.2.3. CM chondrite source for clast mIM in howardite GRO 95574

A few olivines in Clast mIM have distinct cores that are more Mg-rich (Fo_{97-99}) than the rest of the olivine ($Fo_{73–88}$), which crystallized from the impact melt. The distinct Mg-rich cores have very low Fe/Mn ratios (=14–17), similar to olivine found in other unmelted carbonaceous chondrite fragments in howardites (Gounelle et al., 2003; Lunning et al., 2016). These relict olivine cores have Fe/Mn ratios much lower than is typical of HED olivine Fe/Mn = 40–60 (e.g., Beck et al., 2012), which indicates this clast was exogenic relative to its host howardite. The rest of the olivines in Clast mIM have relatively high Fe/Mn ratios (64–126), which are similar to the non-relict olivines ($Fo_{50–85}$ and Fe/Mn = 60–140) in CV impact melt clasts in this study (Clasts A, B, C, and Z). Additionally, low Fe/Mn ratios in Mg-rich olivine relict cores are consistent with some chondritic debris recognized in lunar breccias (Joy et al., 2012) and with Mg-rich olivine in CM chondrites (Frank et al., 2014).

The bulk elemental composition of Clast mIM is broadly consistent with its formation from a carbonaceous chondrite precursor: it has high Al/Si = 0.146 and Ca/Si = 0.138 ratios combined with relatively low Na/Ca = 0.259 and Mn/Al = 0.109 ratios. The Al/Si and Ca/Si ratios of Clast mIM are a slightly higher than those found in any chondrite group; CV and CM chondrites have among the highest Al/Si and Ca/Si ratios. Its Na/Ca and Mn/Al ratios fall within the ranges of bulk elemental compositions of CM and CO chondrites (Tables 1 and 6).

In situ oxygen three-isotope analyses of olivine provide a further test of the provenance of Clast mIM. The relict core has a very primitive O isotopic signature, which falls slightly above to the carbonaceous chondrite anhydrous minerals (CCAM) line (Fig. 4) and close to the Primitive Chondrule Mineral (PCM) line defined by Ushikubo et al. (2012). The cores of unequilibrated olivine grains without relict cores have oxygen isotopic compositions that coincide with bulk CM chondrite values (Fig. 4). It is not clear how degassing of O-bearing volatile species related to impact melting of carbonaceous chondrite targets on airless bodies might fractionate oxygen isotopes. If O-bearing volatile species did not degas, or if O-isotope exchange between volatile-rich impact-generated gas and chondrite-like melt was efficient (e.g., Yu et al., 1995), without additional constraints, we would expect minerals that grew from the melt to have oxygen three-isotope signature of the bulk melt. Oxygen isotope diffusion is slower in olivine than in glass (e.g., Gérard and Jaoul, 1989; Kita et al., 2010): Olivine may better preserve the oxygen-three isotope signature of the original melt. Although Clast mIM is not a chondrule based on the evidence presented in Section 4.1.1, chondrules provide relevant analogs for oxygen isotope homogeneity during rapid cooling and crystallization from a mm-sized melt droplet such as Clast mIM. Excluding relict cores of phenocrysts, the separate phenocrysts of olivine and/or pyroxene as well as mesostasis within an individual chondrule typically have the same oxygen three-isotope signatures (Kita et al., 2016 synthesis of data from Kita et al., 2008, 2010, 2015; Rudraswami et al., 2011; Tenner et al., 2013; Tenner et al. 2015a,b; Weisberg et al., 2010, 2011; Ushikubo et al., 2012). Based on the internal oxygen three-isotope homogeneity found in chondrules, we may reasonably infer distinct oxygen three-isotope signatures from the non-relict olivine in Clast mIM. The simplest explanation for the oxygen three-isotope signatures of the non-relict-bearing olivine microphenocrysts in Clast mIM grew from a melt with a bulk CM chondrite oxygen three-isotope signature.

The contact between Clast mIM and its host meteorite provides textural evidence that this clast formed as a melt droplet: (1) Most olivines along the edge of the clast are

complete euhedral–subhedral crystals, and only a few olivines are fractured. (2) The boundary of Clast mIM is relatively smooth and does not interfinger with the clastic matrix of the host regolithic howardite GRO 95574. (3) The roughly equidimensional shape of Clast mIM is consistent with its being a cross section of a spherical droplet (Fig. 1 and Supplementary Figs. 12 and 13). Thus, Clast mIM probably formed in a manner similar to that of impact melt droplets identified from other solar system bodies, such as lunar crystal-bearing spherules (Symes et al., 1998; Ruzicka et al., 2000), a vitrophyre found in the martian regolith breccia NWA 7034 (Udry et al., 2014), and impact spherules identified on the surface of Mars by the Curiosity rover (Minitti et al., 2013). Chondritic impact melts may exist in the regolith of other differentiated bodies: clast T8 in lunar regolith breccia PCA 02007, described and interpreted as a chondrule fragment by Joy et al. (2012), may instead be a fragment of primitive chondrite impact melt based on its olivine three-oxygen isotope signatures (Joy et al., 2012) and petrographic similarity to the clasts in this study. Clast mIM was likely ejected from a larger impactor, because mm-scale impactors do not melt upon impact. Even on the Moon, mm-size impactors are not expected to melt upon impact (e.g., McSween, 1976; Zolensky, 1997). Impactors collide at higher velocities with the Moon than with 4 Vesta, respectively; average impactor velocities of 15 km/s and 5 km/s are based on their respective distances from the Sun (Pieters et al., 2012). At least a few relatively large CR and CM chondrite impactors accreted to 4 Vesta (De Sanctis et al., 2012; McCord et al., 2012; Prettyman et al., 2012; Reddy et al., 2012). Given this context, the bulk silicate composition of Clast mIM (Tables 1 and 6) and its olivine oxygen three-isotope values suggest a CM chondrite precursor for Clast mIM.

4.3. Evidence for volatile loss

Impact melt clasts from CV_{red}, CV_{oxA}, and CM chondrite precursors contain evidence for volatile loss—namely, the absence of evidence for H_2O where H_2O would be expected, and the presence of vesicles. None of the clasts contain glass (when present) with H_2O concentrations above the detection limit of ~2 wt.% (Table 4). Unmelted CM chondrites have H_2O concentrations (water equivalent H) between 6.5 and 12.5 wt.% (Wasson and Kallemeyn, 1988; Jarosewich, 1990; Baker et al., 2002). Consequently, the below-detection H_2O concentrations of the glass in Clast mIM (CM chondrite impact melt clast) suggest that several wt.% of H_2O was lost from this clast before it solidified. Unmelted CV chondrites have H_2O concentrations around or below (0–2.5 wt.% H_2O: Wasson and Kallemeyn, 1988; Jarosewich, 1990), which is near or below the detection limit.

Clast Z, which formed from a CV_{red} precursor, contains distinct vesicles. Of the clasts that likely formed from a CV_{oxA} precursor, Clast B contains distinct vesicles, and Clasts C and A may contain vesicles. Vesicles provide direct evidence that a volatile-bearing melt formed and subsequently degassed; however, in low-gravity environments only minuscule amounts ($\geqslant$10 s of ppm CO–CO_2 or $\geqslant$100 s of ppm H_2O for parent body depths $\leqslant$5 km) of volatiles are required to form vesicles (McCoy et al., 2006). The specific volatile(s) that formed the vesicles in the CV chondrite impact melts are unknown, potentially include but are not limited to H_2O, S_2, and possibly CO–CO_2. CV chondrites do not contain large quantities of bulk C ($\leqslant$0.8 wt.% C: Jarosewich, 1990) from which CO–CO_2 species would form.

Ordinary chondrite impact melts provide analogous case studies of impact melting, albeit of more reduced and typically less volatile-rich precursor material than the impact melt clasts in this study. Vesicles occur in a few ordinary chondrite impact melts (e.g., Benedix et al., 2008), but most ordinary chondrite impact melts are not vesicular (e.g., Rubin et al., 1983; Bogard et al., 1995; Herd et al., 2013). In the case of the vesicular L chondrite impact melt rock PAT 91501, vesicles formed by release of S_2 gas because they are spatially (3-dimensionally) associated with FeNiS globules (Benedix et al., 2008). Rubin and Moore (2011) described vesicles spatially (2-dimensionally) associated with FeNiS in an LL-impact melt breccia, LAR 06299.

4.4. Redox state of impact melt clasts

Degassing of H_2O and/or CO–CO_2 should reduce the oxygen fugacity of an impact melt relative to that of its precursor. Unmelted CV chondrites have intrinsic oxygen fugacities ranging from near the iron-wüstite (IW) buffer to less than a log unit below the quartz–magnetite–fayalite (~QMF-1) buffer (Righter and Neff, 2007). The reduced CV chondrites should have redox states at the lower end, whereas the oxidized CV chondrites should have redox states toward the higher end of this range. The intrinsic oxygen fugacities of unmelted CM chondrites have not been thermodynamically quantified; however, their mineralogy suggests that CM chondrites have higher intrinsic oxygen fugacities than CV chondrites (Rubin et al., 1988).

The most apparent manifestation of intrinsic oxygen and sulfur fugacities in our impact melt clasts is related to the partitioning of Fe between the coexisting silicate and FeNiS liquids. Clasts with higher intrinsic oxygen fugacities should have proportionally less Fe^0 in the FeNiS liquid and more oxidized Fe in the silicate liquid, as FeO and possibly Fe_2O_3.

4.4.1. Evidence regarding redox state from silicates

The FeO_T (total iron expressed as FeO) concentrations of the glass in Clast Z and Clast mIM may reflect relative intrinsic oxygen fugacities inherited from their precursors. These two impact melt clasts are respectively interpreted to have formed from CV_{red} and CM chondrites. Their glass compositions may reasonably be compared to each other because they were quenched at similar points in their crystallization: they have similar proportions of olivine:glass (61:39 and 63:37: Table 2) and similar zoning trends in their olivines (cores ~Fo_{85} to rims $Fo_{75–73}$: Table 3). The glass in Clast mIM (CM impact melt) has 24.7 wt.% FeO_T while the glass in Clast Z (CV_{red} impact melt) has 15.9 wt.% FeO_T. Given that these clasts are petrologically similar otherwise,

the more FeO_T-rich glass in the CM impact melt likely reflects the relatively higher intrinsic oxygen fugacity of its CM chondrite precursor.

The impact melt clasts from the CV_{oxA} were all quenched from a point where a larger proportion of olivine had crystallized, and therefore cannot qualitatively be compared to the CV_{red} and CM chondrite impact melt clasts. However, Clast C contains both FeO_T-rich plagioclase and glass from which we can attempt to estimate oxygen fugacity from the partition coefficient $D_{plag/melt} = (FeO_T$ in plagioclase) /(FeO_T in melt). Phinney (1992) experimentally determined that FeO_T in plagioclase is an oxybarometer because it tracks the proportion of Fe_2O_3 to FeO in the melt, as Fe^{3+} fits more readily into the plagioclase crystal structure. In Clast C, $D_{plag/melt} = 0.09$ which corresponds to QMF+2 under the conditions of Phinney's (1992) experiments. QMF+2 is a higher intrinsic oxygen fugacity than is calculated for its unmelted precursor (IW < CV chondrite ⩾ QMF-1: Righter and Neff, 2007). Phinney's (1992) experiments were run in equilibrium with basaltic liquids at 1180 °C and 1 atm. Clast C formed from a more ultramafic liquid (Table 1), it crystallized under disequilibrium conditions, and we do not know the pressure and temperature conditions of formation.

4.4.2. Evidence regarding redox state from FeNiS globules

The composition and volumetric abundance of FeNiS liquid will be controlled by the redox state of the impact melt. For instance, in melts with lower oxygen fugacity, a greater percentage of the bulk Fe will partition into the FeNiS liquid rather than into the silicate liquid. Melts in this case will contain larger volumes of FeNiS liquid and compositionally FeNiS liquids will be more Fe-rich (relatively more Ni- and S-poor). Thus, oxygen fugacity should influence the proportion of metal to sulfides in FeNiS globules and their respective Ni-concentrations. However, redox state interpretations from the FeNiS globules in these melt clasts should be treated with caution for two reasons:

(1) The immiscibility and greater density of FeNiS liquid relative to silicate liquid means that a given two-dimensional thin section through a clast may not contain a representative proportion of FeNiS globules.
(2) Different FeS (±Ni, Cu, etc.) globules within a single terrestrial magma body do not consistently have the same composition. For instance, in terrestrial magmas FeNiCuS globules that exsolved and coalesced early can have distinct compositions, relative to globules that exsolved later (Fonesca et al., 2008). Thus, the FeNiS globules in each of our samples may not be perfectly representative of the overall FeNiS immiscible liquid in the clast. With these caveats in mind, we can only make broad inferences regarding redox state using FeNiS globules. From our samples, we examine oxygen fugacity via speciation of Fe, as a proxy. However, the correspondence of oxygen fugacity to the valence (oxidation state) and speciation of Fe is rooted in phase equilibria (e.g., Herd, 2008), and these melt clasts formed under disequilibrium conditions.

The mineral phases in the FeNiS globules, along with their chemistries and abundances, may also track a relative increase in intrinsic oxygen fugacity from the CV_{red} impact melt to the CV_{oxA} and CM impact melts. The CV_{red} impact melt (Clast Z) has FeNiS globules that are distinct from those in the CV_{oxA} and CM impact melt clasts. The mineralogies and chemistries of the FeNiS globules in the CV_{oxA} and CM impact melt clasts (Clast A, B, C, and mIM) overlap each other. The CV_{red} impact melt contains troilite and FeNi-metal that zones from ~9 to 27 wt.% Ni. While the CV_{oxA} and CM impact melts also contain a pyrrhotite MSS phase, their FeNi-metals are more Ni-rich, with some as high as 50 wt.% Ni (stoichiometry consistent with tetrataenite), and some of their globules also contain Ni-rich sulfides, including pentlandite. Additionally, the proportion of metal relative to sulfide is greater in FeNiS globules in CV_{red} impact melt clasts (>50% metal) than in FeNiS globules in the CV_{oxA} and CM impact melt clasts (⩽15% metal). The more Ni-rich metal composition and smaller proportion of metal in FeNiS globules in the CV_{oxA} and CM impact melt clasts are consistent with higher intrinsic oxygen fugacities and greater proportions of Fe in their silicate fractions. Conversely, the higher proportion of metal in FeNiS globules and the lower Ni-concentration of the metal in the CV_{red} impact melt clasts are consistent with a relatively lower intrinsic oxygen fugacity. By these qualitative metrics, differences between intrinsic oxygen fugacity between the CV_{oxA} and CM impact melt clasts cannot be recognized, but the CV_{red} impact melt clast has a recognizably lower intrinsic oxygen fugacity. Degassing of several wt.% H_2O from the CM impact melt clast may have reduced the intrinsic oxygen fugacity, to the point that it was close to that of CV_{oxA} chondrites.

4.5. Potential for observation of impact melt on CM chondrite-like asteroids

The mineral assemblages in the impact melt clasts in this study are distinctly different from those in their precursors. Such changes in mineralogy could potentially be observed with visible/infrared spectroscopy via remote sensing to identify impact melt-rich regions on the surfaces of asteroids, particularly on the surfaces of CM chondrite-like bodies. Unmelted CM chondrites have spectra dominated by absorption features related to their phyllosilicates (Cloutis et al., 2011; Takir et al., 2013; Beck et al., 2014b). In contrast, the CM impact melt clast in this study is composed primarily of olivine and glass. The spectra of glasses are relatively featureless, although glass can alter a spectrum's continuum (Cloutis et al. 1990); thus olivine absorption features would dominate spectra of CM chondrite impact melts. Specifically, olivine has a broad absorption feature which typically extends ~0.9 to 1.25 μm (e.g., Cloutis et al. 2011) and an absorption feature at ~11.3 μm (Beck et al. 2014b). Laboratory spectra of CM chondrites typically do not show the ~0.9 to 1.25 μm absorption feature of olivine (Cloutis et al. 2011). Occasionally CM chondrites have a weak ~11.3 μm absorption feature but in this spectral range CM chondrites have a more prominent ~9.9 μm feature associated with phyllosilicates

(Beck et al. 2014b; McAdam et al. 2015). These hydrated minerals are also apparent in other spectral ranges: OH and H_2O related absorption features at ~3 μm (e.g., Takir et al. 2013) and an Fe^{2+} to Fe^{3+} charge transfer transition absorption at ~0.7 μm (Vilas and Gaffey 1989). However, the ~0.7 μm absorption feature is relatively weak, is only present in phyllosilicates that contain oxidized Fe, and is, therefore, sometimes absent in the spectra of CM chondrites with abundant phyllosilicates (McAdam et al. 2015).

Using ground-based observations in which a spectrum averages the composition over the entire visible hemisphere/area, we posit that a CM chondrite-like asteroid with abundant impact melt on its surface would have a spectrum with phyllosilicate-related absorption features and stronger olivine absorption features than typically observed in the spectra of unmelted CM chondrite material. In a composite spectrum viewed from Earth, it would be difficult to distinguish a combination of impact melt and CM chondrite material from CM chondrite material combined with olivine-rich material of another provenance, such as CM chondrites metamorphosed to higher temperatures than we observe in meteorites or such as exogenic material from other olivine-rich meteorite groups (includes unmelted CV chondrites, Beck et al., 2014b). However, it is reasonable to expect that impact melt on CM chondrite-like asteroids may not necessarily constitute a large enough fraction of the visible area to contribute absorption features to a spectrum observed from Earth. Resolving impact melt from unmelted CM chondrite material may require higher spatial resolution mapping of CM chondrite-like asteroids by spacecraft.

Two spacecraft missions, NASA's Osiris-Rex and JAXA's Hayabusa 2, will map and return samples from asteroids for which CM chondrites are appropriate meteorite analogs. The target of Osiris-Rex is near-Earth asteroid (101955) Bennu, which has spectra most similar to CM and CI chondrites but without any observed absorption features related to hydrated phases such as phyllosilicates (Clark et al. 2011; Lauretta et al. 2015; Binzel et al. 2015), although it has not been observed in the 3-μm region where phyllosilicate absorptions are strongest. Ryugu 708 (formerly Asteroid (162173) 1999 JU3)—the target of Hayabusa 2—is also spectrally similar to CM and CI chondrites (Vilas 2008; Moskovitz et al. 2013). A ~0.7 μm absorption feature has been observed in spectra from Hayabusa 2's target, albeit not consistently (Vilas 2008; Lazzaro et al. 2013). Moskovitz et al. (2013) proposed that the ~0.7 μm absorption feature may not be consistently observable if either 1) this asteroid has a heterogeneous surface composition or 2) the asteroid's orbital proximity to the Sun influences the manifestation of the ~0.7 μm absorption feature. Subsequent work looked for but did not find any orbital elements correlated to the presence of ~0.7 μm absorption feature on carbonaceous chondrite-like asteroids (Fornasier et al. 2014). If Ryugu 708 has had a complex collisional history, it might have olivine-rich impact melt on its surface.

Although Vesta is a differentiated asteroid, it contains exogenic carbonaceous chondrite material mixed into its surface regolith (McCord et al. 2012; De Sanctis et al. 2012; Reddy et al. 2012; Prettyman et al. 2012; Jaumann et al. 2014). Olivine-rich lithologies have been identified in geologically unexpected locations on Vesta (e.g., Ammannito et al. 2013; Le Corre et al. 2015). The CM chondrite impact melt in howardite GRO 95574 identified and described in this work—Clast mIM—has been discussed as a possible analog for these olivine-rich areas on Vesta (Nathues et al. 2014; Thangjam et al. 2014; Poulet et al. 2015), based on preliminary conference presentations (Lunning et al. 2014; Beck et al., 2014a) of data presented in this paper.

5. SUMMARY AND CONCLUSIONS

Scott et al. (1992) speculated that impact melts from CM and CV chondrites did not exist, because of the lack of recognized samples and because the potential explosivity of their impact melts might prevent cohesive melt from forming. We identify and describe five CV and CM chondrite impact melt clasts, each of which has a slightly different petrogenesis. These five impact melt clasts formed from three separate carbonaceous chondrite precursors based on their silicate bulk elemental composition and individual petrology:

1. A melt pocket formed from a $CV3_{red}$ chondrite precursor (Clast Z in RBT 04143) melted *in situ* based on its texture, and has bulk silicate elemental composition consistent with that of a CV chondrite.
2. Three clasts formed from $CV3_{oxA}$ chondrite precursor material (Clasts A, B, C in LAR 06317) and experienced different degrees of crystallization prior to final solidification. The fragmented olivine crystals that define the clast boundaries of all three clasts indicate that they were brecciated after solidification. Their bulk silicate elemental compositions are consistent with those of CV chondrites, and thus their $CV3_{oxA}$ chondrite host is probably representative of their precursor.
3. One melt droplet interpreted to have formed from a CM chondrite precursor (Clast mIM in howardite GRO 95574) solidified as an ejected molten droplet from a larger impactor and after solidification was incorporated into a regolithic howardite. The oxygen three-isotope signatures and Fe/Mn values of its olivine distinguish this clast from howardite-eucrite-diogenite materials. The oxygen three-isotope signatures of relict olivine and olivines that grew from the melt provide evidence that this clast formed from a primitive (most likely CM) chondrite.

Evidence for degassing in all three types of carbonaceous chondrite impact melts in this study is presented. Impact melt clasts that we interpret formed from $CV3_{red}$ chondrite and $CV3_{oxA}$ chondrite precursors contain vesicles. The glass in impact melt that formed from a CM chondrite precursor has an H_2O-concentration below our Raman spectroscopy detection limits, which indicates it lost several wt.% H_2O relative to its precursor. Depending on which species degassed, H_2O loss could potentially reduce

the intrinsic oxygen fugacity. However, our observations suggest that the relative redox states of the $CV3_{red}$ and $CV3_{oxA}$ chondrite melt clasts are comparable to their precursors'.

The petrologic features of the clasts in this study may potentially be used to spectroscopically identify carbonaceous chondrite impact melt lithologies on asteroid surfaces.

ACKNOWLEDGMENTS

We thank the Meteorite Working Group, NASA Johnson Space Center and the Smithsonian Institution for allocation of thin sections, Allan Patchen for assistance with EMPA, Charles Farley for assistance with Raman spectroscopy, and Tim Gooding for advice regarding nanoSEM analyses and sample preparation. We thank Josh Emery, Ted Labotka, and Tim McCoy for thought provoking discussions throughout this project. We thank our reviewers, Alan Rubin, Michael Zolensky, and Katherine Joy, for constructive comments. We thank Dr. Gregory Herzog for careful editorial handling. Additional information and data, including supplementary figures and tables, are available in the Electronic Annex. This research was supported in part by NASA through Cosmochemistry Grants NNX13AH86G to HYM and NNX11AG62G to NTK. WiscSIMS is partly supported by NSF (EAR10-53466).

APPENDIX A. SUPPLEMENTARY DATA

Supplementary data associated with this article can be found, in the online version, at http://dx.doi.org/10.1016/j.gca.2016.05.038.

REFERENCES

Ammannito E., De Sanctis M. C., Palomba E., Longobardo A., Mittlefehldt D. W., McSween H. Y., Marchi S., Capria M. T., Capaccioni E., Frigeri A., Pieters C. M., Ruesch O., Tosi T., Zambon F., Carroro F., Fonte S., Hiesinger H., Magni G., McFadden L. A., Raymond C. A., Russell C. T. and Sunshine J. M. (2013) Olivine in an unexpected location on Vesta's surface. *Nature* **504**, 122–125.

Asphaug E., Jutzi M. and Movshovitz N. (2011) Chondrule formation during planetesimal accretion. *Earth Planet. Sci. Lett.* **308**, 369–379.

Baker L., Franchi I. A., Wright I. P. and Pillinger C. T. (2002) The oxygen isotopic composition of water from Tagish Lake: its relationship to low-temperature phases and to other carbonaceous chondrites. *Meteorit. Planet. Sci.* **43**, 977–985.

Beck A. W., Welten K. C., McSween H. Y., Viviano C. E. and Caffee M. W. (2012) Petrologic and textural diversity among the PCA 02 howardite group, one of the largest pieces of the vestan surface. *Meteorit. Planet. Sci.* **47**, 947–969.

Beck A. W., Lunning N. G., De Sanctis M. C., Hiroi T., Plescia J., Viviano-Beck C. E., Udry A., Corrigan C. M. and McCoy T. J. (2014a) A meteorite analog for olivine-rich terrain in unexpected locations on Vesta. *Lunar Planet. Sci. XLV Lunar Planet. Inst. Houston*, #2499 (abstr.).

Beck P., Garenne A., Quirico E., Bonal L., Montes-Hernadez G., Moynier F. and Schmitt B. (2014b) Transmission infrared spectra (2–25 microns) of carbonaceous chondrites (CI, CM, CV-CK, CR, C2 ungrouped): mineralogy, water, and asteroidal processes. *Icarus* **229**, 263–277.

Benedix G. K., Ketcham R. A., Wilson L., McCoy T. J., Bogard D. D., Garrison D. H., Herzog G. F., Xue S., Klein J. and Middleton R. (2008) The formation and chronology of the PAT 91501 impact-melt L chondrite with vesicle-metal-sulfide assemblages. *Geochim. Cosmochim. Acta* **72**, 2417–2428.

Binzel R. P., DeMeo F. E., Burt B. J., Cloutis E. A., Rozitis B., Burbine T. H., Campins H., Clark B. E., Emery J. P., Hergenrother C. W., Howell E. S., Lauretta D. S., Nolan M. C., Mansfield M., Pietrasz V., Polishook D. and Scheeres D. J. (2015) Spectral slope variations for OSIRIS-REx target Asteroid (101955) Bennu: possible evidence for a fine-grained regolith equatorial ridge. *Icarus* **256**, 22–29.

Bischoff A. and Stöffler D. (1992) Shock metamorphism as a fundamental process in the evolution of planetary bodies: information from meteorites. *Eur. J. Mineral.* **4**, 707–755.

Bischoff A., Scott E. R. D., Metzler K. and Goodrich C. A. (2006) Nature and origin of meteorite breccias. In *Meteorite and the Early Solar System II* (eds. D. S. Lauretta and , Jr.H. Y. McSween). University of Arizona Press, Tucson, pp. 670–712.

Bogard D. D., Garrison D. H., Norman M., Scott E. R. D. and Keil K. (1995) ^{39}Ar-^{40}Ar age and petrology of Chico: large-scale impact-melting on the L chondrite parent body. *Geochim. Cosmochim. Acta* **59**, 1383–1399.

Bogard D. D. (2011) K-Ar ages of meteorites: clues to parent-body thermal histories. *Chem. Erde* **71**, 207–226.

Brearley A. J. and Jones R. H. (1998) Chondritic meteorites. In *Reviews in Mineralogy*, vol. 36 (ed. J. J. Papike). Mineralogical Society of America, Washington, pp. 3-1-3-398.

Buchanan P. C., Zolensky M. E. and Reid A. M. (1993) Carbonaceous chondrite clasts in the howardites Bholghati and EET 87513. *Meteoritics* **28**, 659–669.

Caillet C., MacPherson G. J. and Zinner E. K. (1993) Petrologic and Al-Mg isotopic clues to the accretion of two refractory inclusions onto the Leoville parent body: one was hot, the other wasn't. *Geochim. Cosmochim. Acta* **57**, 4725–4743.

Cartwright J. A., Ott U. and Mittlefehldt D. W. (2014) The quest for regolithic howardites. Part 2: surface origins highlighted by noble gases. *Geochim. Cosmochim. Acta* **140**, 488–508.

Clark B. E., Binzel R. P., Howell E. S., Cloutis E. A., Ockert-Bell M., Christensen P., Barucci M. A., DeMeo F., Lauretta D. S., Connolly H., Soderberg A., Hergenrother C., Lim L., Emery J. and Mueller M. (2011) Asteroid (101955) 1999 RQ36: spectroscopy from 0.4 to 2.4 μm. *Icarus* **216**, 462–475.

Cloutis E. A., Gaffey M. J., Smith D. G. W. and Lambert R. S.-J. (1990) Reflectance spectra of glass-bearing mafic silicate mixture and spectral deconvolution procedures. *Icarus* **86**, 383–401.

Cloutis E. A., Hudon P., Hiroi T., Gaffey M. J. and Mann P. (2011) Spectral reflectance properties of carbonaceous chondrites: 2. CM chondrites. *Icarus* **216**, 309–346.

Connolly H. C. and Desch S. J. (2004) On the origin of the "kleine Kügelchen" called Chondrules. *Chem. Erde* **64**, 95–125.

Day J. M. D., Walker R. J., Ash R. A., Liu Y., Rumble D., Irving A. J., Goodrich C. A., Tait K., McDonough W. F. and Taylor L. A. (2012) Origin of felsic achondrites Graves Nunataks 06128 and 06129, and ultramafic brachinites and brachinite-like achondrites by partial melting of volatile-rich primitive parent bodies. *Geochim. Cosmochim. Acta* **81**, 94–128.

De Sanctis M. C., Ammannito E., Capria M. T., Tosi F., Capaccioni F., Zambon F., Carraro F., Fonte S., Frigeri A., Jaumann R., Magni G., Marchi S., McCord T. B., McFadden L. A., McSween H. Y., Mittlefehldt D. W., Nathues A., Palomba E., Pieters C. M., Raymond C. A., Russell C. T., Toplis M. J. and Turrini D. (2012) Spectroscopic characterization of mineralogy and its diversity across Vesta. *Science* **338**, 697–700.

Dodd R. T., Jarosewich E. and Hill B. (1982) Petrogenesis of complex veins in the Chantonnay (L6f) chondrite. *Earth Planet. Sci. Lett.* **59**, 364–374.

Dodd R. T. and Jarosewich E. (1982) The compositions of incipient shock melts in L6 chondrites. *Earth Planet. Sci. Lett.* **59**, 355–363.

Dunn T. L. and Gross J. (2015) Magnetite in CK and CV chondrites: evidence for two parent bodies? *Lunar and Planet. Sci. XLVI Lunar Planet. Inst. Houston*, #1105 (abstr.).

Fazio A., D'Orazio M., Cordier C. and Folco L. (2016) Target-projectile interaction during impact melting at Kamil Crater, Egypt. *Geochim. Cosmochim. Acta* **180**, 33–50.

Feldstein S. N., Jones R. H. and Papike J. J. (2001) Disequilibrium partial melting experiments on Leedey L6 chondrite: textural controls on melting processes. *Meteorit. Planet. Sci.* **36**, 1421–1441.

Fonseca R. O. C., Campbell I. H., O'Neill H. S.-C. and Fitzgerald J. D. (2008) Oxygen solubility and speciation in sulphide-rich mattes. *Geochim. Cosmochim. Acta* **72**, 2619–2635.

Fornasier S., Lantz C., Barucci M. A. and Lazzarin M. (2014) Aqueous alteration on main belt primitive asteroids: results from visible spectroscopy. *Icarus* **233**, 163–178.

Frank D. R., Zolensky M. E. and Le L. (2014) Olivine in terminal particles of Stardust aerogel tracks and analogous grains in chondrite matrix. *Geochim. Cosmochim. Acta* **142**, 240–259.

Friedrich J. M., Weisberg M. K., Ebel D. S., Biltz A. E., Corbett B. M., Iotzov I. V., Khan W. S. and Wolman M. D. (2015) Chondrule size and related physical properties: a compilation and evaluation of current data across all meteorite groups. *Chem. Erde* **75**, 419–443.

Gardner-Vandy K. G., Lauretta D. S., Greenwood R. C., McCoy T. J., Killgore M. and Franchi I. A. (2012) The Tafassasset primitive achondrite: insights into initial stages of planetary differentiation. *Geochim. Cosmochim. Acta* **85**, 142–159.

Gérard O. and Jaoul O. (1989) Oxygen diffusion in San Carlos Olivine. *J. Geophys. Res.* **94**, 4119–4128.

Gounelle M., Zolensky M. E., Liu J.-C., Bland P. A. and Alard O. (2003) Mineralogy of carbonaceous chondritic microclasts in howardites: identification of C2 fossil micrometeorites. *Geochim. Cosmochim. Acta* **67**, 507–527.

Greenwood R. C., Franchi I. A., Kearsley A. T. and Alard O. (2010) The relationship between CK and CV chondrites. *Geochim. Cosmochim. Acta* **74**, 1684–1705.

Grossman J. N., Rubin A. E., Nagahara H. and King E. A. (1988) Properties of chondrules. In *Meteorites and the Early Solar System* (eds. J. F. Kerridge and M. S. Matthews). University of Arizona Press, Tuscon, pp. 488–511.

Herd C. D. K. (2008) Basalts as probes of planetary interior redox state. *Rev. Mineral. Geochem.* **68**, 527–553.

Herd C. D. K., Friedrich J. M., Greenwood R. C. and Franchi I. A. (2013) An igneous-textured clast in the Peace River meteorite: insights into accretion and metamorphism of asteroids in the early solar system. *Can. J. Earth Sci.* **50**, 14–25.

Hewins R. H. (1997) Chondrules. *Annu. Rev. Earth Planet. Sci.* **25**, 61–83.

Ishida H., Nakamura T., Miura H. and Kakzu Y. (2012) Diverse mineralogical and oxygen isotopic signatures recorded in CV3 carbonaceous chondrites. *Polar Sci.* **6**, 252–262.

Jaumann R., Williams D. A., Buczkowski D. L., Yingst R. A., Preusker F., Hiesinger H., Schmedemann N., Kneissl T., Vincent J. B., Blewett D. T., Buratti B. J., Carsenty U., Denevi B. W., De Sanctis M. C., Garry W. B., Keller H. U., Kersten E., Krohn K., Li J.-Y., Marchi S., Matz K. D., McCord T. B., McSween H. Y., Mest S. C., Mittlefehldt D. W., Mottola S., Nathues A., Neukum G., O'Brien D. P., Pieters C. M., Prettyman P., Raymond C. A., Roatsch T., Russell C. T., Schenk P., Schmidt B. E., Scholten F., Stephan K., Skyes M. V., Tricarico P., Wagner R., Zuber M. T. and Sierks H. (2012) Vesta's shape and morphology. *Science* **336**, 687–690.

Jaumann R., Nass A., Otto K., Krohn K., Stephan K., McCord T. B., Williams D. A., Raymond C. A., Blewett D. T., Hiesinger H., Yingst R. A., De Sanctis M. C., Palomba E., Roatsch T., Matz K.-D., Preusker F., Scholten F. and Russell C. T. (2014) The geological nature of dark material on Vesta and implications for the subsurface structure. *Icarus* **240**, 3–19.

Jarosewich E. (1990) Chemical analyses of meteorites: a compilation of stony and iron meteorite analyses. *Meteoritics* **25**, 323–337.

Johnson B. C., Minton D. A., Melosh H. J. and Zuber M. T. (2015) Impact jetting as the origin of chondrules. *Nature* **517**, 339–341.

Johnson C. A. and Prinz M. (1991) Chromite and olivine in type II chondrules in carbonaceous and ordinary chondrites: implications for thermal histories and group differences. *Geochim. Cosmochim. Acta* **55**, 893–904.

Joy K. H., Zolensky M. E., Nagashima K., Huss G. R., Ross D. K., McKay D. S. and Kring D. A. (2012) Direct detection of projectile relics from the end of the lunar basin-forming epoch. *Science* **336**, 1426–1429.

Kallemeyn G. W., Rubin A. E. and Wasson J. T. (1991) The compositional classification of chondrites: V. The Karoonda (CK) group of carbonaceous chondrites. *Geochim. Cosmochim. Acta* **55**, 881–892.

Kallemeyn G. W., Rubin A. E. and Wasson J. T. (1994) The compositional classification of chondrites: VI. The CR carbonaceous chondrite group. *Geochim. Cosmochim. Acta* **58**, 2873–2888.

Kita N. T., Kimura M., Ushikubo T., Valley J. W. and Nyquist L. E. (2008) Oxygen isotope systematics of chondrules from the least equilibrated H chondrite. *Lunar and Planet. Sci. XXXIX Lunar Planet. Inst. Houston*, #2059 (abstr.).

Kita N. T., Nagahara H., Tachibana S., Tomomura S., Spicuzza M. J., Fournelle J. H. and Valley J. W. (2010) High precision SIMS oxygen three isotope study of chondrules in LL3 chondrites: role of ambient gas during chondrules formation. *Geochim. Cosmochim. Acta* **74**, 6610–6635.

Kita N. T., Tenner T. J., Defouilloy C., Nakashima D., Ushikubo T. and Bischoff A. (2015) Oxygen isotope systematics of chondrules in R3 clasts: A genetic link to ordinary chondrites. *Lunar and Planet. Sci. XLVI Lunar Planet. Inst. Houston*, #2053 (abstr.).

Kita N. T., Tenner T. J., Ushikubo T., Nakashima D., Rudraswami N. G., Weisberg M. K., Defouilloy C., Kimura M., Nagahara H. and Bischoff A. (2016) Internal homogeneity of oxygen isotope ratio in chondrules. *Lunar and Planet. Sci. XLVII Lunar Planet. Inst. Houston*, #2375 (abstr.).

Krot A. N., Keil K., Scott E. R. D., Goodrich C. A. and Weisberg M. K. (2003) Chapter 1.05 Classification of meteorites. In *Meteorites, Comets, and Planets*, vol. 1 (ed. A. M. Davis), pp. 1–52. Treatise on Geochemistry. Elsevier, Amsterdam.

Lazzaro D., Barucci M. A., Perna D., Jasmin F. L., Yoshikawa M. and Carvano J. M. F. (2013) Rotational spectra of (162173) 1999 JUE, the target of the Hayabusa2 mission. *Astron. Astrophys.* **549**, L2.

Lauretta D. S., Bartels A. E., Barucci M. A., Bierhaus E. B., Binzel R. P., Bottke W. F., Campins H., Chesley S. R., Clark B. C., Clark B. E., Cloutis E. A., Connolly H. C., Crombie M. K., Delbó J. P., Dworkin J. P., Emery J. P., Glavin D. P., Hamilton V. E., Hergenrother C. W., Johnson C. L., Keller L. P., Michel P., Nolan M. C., Sandford S. A., Scheeres D. J., Simon A. A.,

Sutter, Vokrouhlický and Walsh K. J. (2015) The OSIRIS-Rex target asteroid (101955) Bennu: constraints on its physical, geological, and dynamical nature from astronomical observations. *Meteorit. Planet. Sci.* **50**, 834–849.

Le Corre L., Reddy V., Sanchez J. A., Dunn T., Cloutis E. A., Izawa M. R. M., Mann P. and Nathues A. (2015) Exploring exogenic sources for the olivine on asteroid (4) Vesta. *Icarus* **258**, 483–499.

Le Losq C., Neuville D. R., Moretti R. and Roux J. (2012) Determination of water content in silicate glasses using Raman spectrometry: implications for the study of explosive volcanism. *Am. Mineral.* **97**, 779–790.

Lofgren G. (1989) Dynamic crystallization of chondrule melts of porphyritic olivine compositions: textures experimental and natural. *Geochim. Cosmochim. Acta* **53**, 461–470.

Lunning N. G., Corrigan C. M., McSween H. Y., Tenner T. J., and Kita N. (2014) CM chondrite impact melt clast identified in a regolithic howardite. Meteorit. Planet. Sci. 49 Annu. Met. Soc. Meeting 77th #5193 (abstr.).

Lunning N. G., McSween H. Y., Tenner T. J., Kita N. K. and Bodnar R. J. (2015) Olivine and pyroxene from the mantle of asteroid 4 Vesta. *Earth Planet. Sci. Lett.* **418**, 126–135.

Lunning N. G., Welten K. C., McSween H. Y., Caffee M. W. and Beck A. W. (2016) Grosvenor Mountains 95 howardite pairing group: insights into the surface regolith of asteroid 4 Vesta. *Meteorit. Planet. Sci.* **51**, 167–194.

McAdam M. M., Sunshine J. M., Howard K. T. and McCoy T. M. (2015) Aqueous alteration on asteroids: linking the mineralogy and spectroscopy of CM and CI chondrites. *Icarus* **245**, 340-332.

McCord T. B., Li L.-Y., Combe J.-P., McSween H. Y., Jaumann R., Reddy V., Tosi F., Williams D. A., Blewett D. T., Turrini D., Palomba E., Pieters C. M., De Sanctis M. C., Ammannito E., Capria M. T., Le Corre L., Longobardo A., Nathues A., Mittlefehldt D. W., Schröder S. E., Hiesinger H., Beck A. W., Capaccioni F., Carsenty U., Keller H. U., Denevi D. W., Sunshine J. M., Raymond C. A. and Russell C. T. (2012) Dark material on Vesta from the infall of carbonaceous volatile-rich material. *Nature* **491**, 83–86.

McCoy T. J., Ketcham R. A., Wilson L., Benedix G. K., Wadhwa M. and Davis A. M. (2006) Formation of vesicles in asteroidal basaltic meteorites. *Earth Planet. Sci. Lett.* **246**, 102–108.

McSween H. Y. (1976) A new type of chondritic meteorite found in lunar soil. *Earth Planet. Sci. Lett.* **31**, 193–199.

McSween H. Y. (1977) Chemical and petrographic constraints on origin of chondrules and inclusion in carbonaceous chondrites. *Geochim. Cosmochim. Acta* **41**, 1843–1860.

McSween H. Y., Binzel R. P., De Sanctis M. C., Ammannito E., Prettyman T. H., Beck A. W., Reddy V., Le Corre L., Gaffey M. J., McCord T. B., Raymond C. A. and Russell C. T.the Dawn Science Team (2013) Dawn; the Vesta-HED connection; and the geologic context for eucrite, diogenites, and howardites. *Meteorit. Planet. Sci.* **48**, 2090–2104.

Metzler K., Bischoff A., Greenwood R. C., Palme H., Gallissen M., Hopp J., Franchi I. A. and Trieloff M. (2011) The L3–6 chondritic regolith breccia Northwest African (NWA) 869 (I) Petrology, chemistry, oxygen isotope, and Ar-Ar age determinations. *Meteorit. Planet. Sci.* **46**, 652–680.

Minitti M. E., Kah L. C., Yingst R. A., Edgett K. S., Anderson R. C., Beegle L. W., Carsten J. L., Deen R. G., Goetz W., Hardgove C., Harker D. E., Herkenhoff K. E., Hurowitz J. A., Jandura L., Kennedy M. R., Kocurek G., Krezoski G. M., Kuhn S. R., Limonadi D., Lipkaman L., Madsen M. B., Olson T. S., Robinson M. L., Rowland S. K., Rubin D. M., Seybold C., Schieber J., Schmidt M., Sumner D. Y., Tompkins V. V., Van Beek and Van Beek T. (2013) MAHLI at the Rocknest sand shadow: science and science-enabling activities. *J. Geophys. Res. E* **118**, 2338–2360.

Mittlefehldt D. W., McCoy T. J., Goodrich C. A. and Kracher A. (1998) Non-chondritic meteorites from asteroidal bodies. In *Reviews in Mineralogy*, vol. 36 (ed. J. J. Papike) (eds. Papike and Papike). Mineralogical Society of America, Washington DC, pp.4-01-4-170.

Mittlefehldt D. W. and Lindstrom M. M. (2001) Petrology and geochemistry of Patuxent Range 91501, a clast-poor impact-melt from the L-chondrite parent body and Lewis Cliff 88663, an L7 chondrite. *Meteorit. Planet. Sci.* **36**, 439–457.

Moskovitz N. A., Abe S., Pan K.-S., Osip D. J., Pefkou D., Melita M. D., Elias M., Kitazato K., Bus S. J., DeMeo F. E., Binzel R. P. and Abell P. A. (2013) Rotational characterization of Hayabusa II target Asteroid (162173) 1999 JU3. *Icarus* **224**, 24–31.

Nathues A., Hoffmann M., Schäfer M., Thanjam G., Le Corre L., Reddy V., Christensen U., Mengel K., Sierks H., Vincent J.-B., Cloutis E. A., Russell C. T., Schäfer T., Gutierrez-Marques P., Hall I., Ripken J. and Büttner I. (2014) Exogenic olivine on Vesta from Dawn framing camera color data. *Icarus* **258**, 467–482.

Phinney W. C. (1992) Partition coefficients for iron between plagioclase and basalt as a function of oxygen fugacity: implications for Archean and lunar anorthosites. *Geochim. Cosmochim. Acta* **56**, 1885–1895.

Pieters C. M., Ammannito E., Blewett D. T., Denevi B. W., De Sanctis M. C., Gaffey M. J., Le Corre L., Li J.-Y., Marchi S., McCord T. B., McFadden L. A., Mittlefehldt D. W., Nathues A., Palmer E., Reddy V., Raymond C. A. and Russell C. T. (2012) Distinctive space weathering on Vesta from regolith mixing processes. *Nature* **491**, 79–82.

Pouchou J. L. and Pichoir F. (1984) A new model for quantitative X-ray microanalysis. I. Application to the analysis of homogeneous samples. *La Recherche Aérospatiale* **5**, 349–367.

Poulet F., Ruesch O., Langevin Y. and Hiesinger H. (2015) Modal mineralogy of the surface of Vesta: evidence for ubiquitous olivine and identification of meteorite analogues. *Icarus* **253**, 364–377.

Prettyman T. H., Mittlefehldt D. W., Yamashita N., Lawrence D. J., Beck A. W., Feldman W. C., McCoy T. M., McSween H. Y., Toplis M. J., Titus T. N., Tricarico P., Reedy R. C., Hendricks J. S., Forni O., Le Corre L., Li Jian-Yan, Mizzon H., Reddy V., Raymond C. A. and Russell C. T. (2012) Elemental mapping by dawn reveals exogenic H in Vesta's regolith. *Science* **338**, 242–246.

Radomsky P. M. and Hewins R. H. (1990) Formation conditions of pyroxene-olivine and magnesian olivine chondrules. *Geochim. Cosmochim. Acta* **54**, 3475–3490.

Reddy V., Le Corre L., O'Brien D. P., Nathues A., Cloutis E. A., Durda D. D., Bottke W. F., Bhatt M. U., Nesvorny D., Buczkowski D., Scully J. E. C., Palmer E. M., Sierks H., Mann P. J., Becker K. J., Beck A. W., Mittlefehldt D., Li J.-Y., Gaskell R., Russell C. T., Gaffey M. J., McSween H. Y., McCord T. B., Combe J.-P. and Blewett D. (2012) Delivery of dark material to Vesta via carbonaceous chondritic impacts. *Icarus* **221**, 544–559.

Righter K. and Neff K. E. (2007) Temperature and oxygen fugacity constraints on CK and R chondrites and implications for water and oxidation in the early solar system. *Polar Sci.* **1**, 25–44.

Rubin A. E. (1985) Impact melt products of chondritic material. *Rev. Geophys.* **23**, 277–300.

Rubin A. E. (1992) A shock-metamorphic model for silicate darkening and compositionally variable plagioclase in CK and

ordinary chondrites. *Geochim. Cosmochim. Acta* **56**, 1705–1714.

Rubin A. E. and Bottke W. F. (2009) On the origin of shocked and unshocked CM clasts in H-chondrite regolith breccias. *Meteorit. Planet. Sci.* **44**, 701–724.

Rubin A. E. and Moore W. B. (2011) What's up? Preservation of gravitational direction in the Larkman Nunatak 06299 LL impact melt breccia. *Meteorit. Planet. Sci.* **46**, 737–747.

Rubin A. E., Rehfeldt A., Peterson E., Keil K. and Jarosewich E. (1983) Fragmental breccias and the collisional evolution of ordinary chondrite parent bodies. *Meteoritics* **18**, 179–196.

Rubin A. E., Fegley B. and Brett R. (1988) Oxidation state in chondrites. In *Meteorites and the Early Solar System* (eds. J. F. Kerridge and M. S. Matthews). The University of Arizona Press, Tuscon, pp. 488–511.

Rudraswami N. G., Ushikubo T., Nakashima D. and Kita N. T. (2011) Oxygen isotope systematics of chondrules in the Allende CV3 chondrite: high precision ion microprobe studies. *Geochim. Cosmochim. Acta* **75**, 7596–7611.

Ruzicka A., Snyder G. A. and Taylor L. A. (1998) Mega-chondrules and large, igneous-textured clasts in Julesberg (L3) and other ordinary chondrites: vapor-fractionation, shock-melting, and chondrule formation. *Geochim. Cosmochim. Acta* **62**, 1419–1442.

Ruzicka A., Snyder G. A. and Taylor L. A. (2000) Crystal-bearing lunar spherules: impact melting of the Moon's crust and implications for the origin of meteoritic chondrules. *Meteorit. Planet. Sci.* **35**, 173–192.

Satterwhite C. and Righter K. (2007) Petrographic descriptions. *Antarct. Meteorit. Newsletter* **30**(2), 18–30.

Satterwhite C. and Righter K. (2008) Petrographic descriptions. *Antarct. Meteorit. Newsletter* **31**(1), 24.

Schenk P., O'Brien D. P., Marchi S., Gaskell R., Preusker F., Roatsch T., Jaumann R., Buczkowski D., McCord T., McSween H. Y., Williams D., Yingst A., Raymond C. and Russell C. (2012) The geologically recent giant impact basins at Vesta's south pole. *Science* **336**, 694–697.

Scott E. R. D. (1982) Origin of rapidly solidified metal-troilite grains in chondrites and iron meteorites. *Geochim. Cosmochim. Acta* **46**, 813–823.

Scott E. R. D. and Krot A. N. (2003) 1.07 Chondrites and their components. In *Meteorites, Comets, and Planets: Treatise on Geochemistry*, vol. 1 (ed. A. M. Davis). Elsevier, Amsterdam, pp. 1–72.

Scott E. R. D., Keil K. and Stöffler D. (1992) Shock metamorphism of carbonaceous chondrites. *Geochim. Cosmochim. Acta* **56**, 4281–4293.

Severs M. J., Azbej T., Thomas J. B., Mandeville C. W. and Bodnar R. J. (2007) Experimental determination of H_2O loss from melt inclusions during laboratory heating: evidence from Raman spectroscopy. *Chem. Geol.* **237**, 258–371.

Stöffler D., Keil K. and Scott E. R. D. (1991) Shock metamorphism of ordinary chondrites. *Geochim. Cosmochim. Acta* **55**, 3845–3867.

Symes S. J. K., Sears D. W. G., Akridge D. G., Huang S. and Benoit P. H. (1998) The crystalline lunar spherules: their formation and implications for the origin of meteoritic chondrules. *Meteorit. Planet. Sci.* **33**, 13–29.

Takir D. and Emery J. P. (2012) Outer main belt asteroids: identification and distribution of four 3-μm spectral groups. *Icarus* **219**, 641–654.

Takir D., Emery J. P., McSween H. Y., Hibbitts C. A., Clark R. N., Pearson N. and Wang A. (2013) Nature and degree of aqueous alteration in CM and CI carbonaceous chondrites. *Meteorit. Planet. Sci.* **48**, 1618–1637.

Teitler S. A., Paque J. M., Cuzzi J. N. and Hogan R. C. (2010) Statistical tests of chondrule sorting. *Meteorit. Planet. Sci.* **45**, 1124–1135.

Tenner T. J., Ushikubo T., Kurahashi E., Kita N. T. and Nagahara H. (2013) Oxygen isotope systematics of chondrules phenocrysts from the CO3.0 chondrite Yamato 81020: evidence for two distinct oxygen isotopes reservoirs. *Geochim. Cosmochim. Acta* **102**, 226–245.

Tenner T. J., Nakashima D., Ushikubo T., Kita N. T. and Weisberg M. K. (2015a) Oxygen isotope ratios of FeO-poor chondrules in CR3 chondrites: Influence of dust enrichment and H_2O during chondrule formation. *Geochim. Cosmochim. Acta* **148**, 228–250.

Tenner T. J., Kimura M. and Kita N. T. (2015b) High-precision SIMS chondrule oxygen isotope ratios from the Yamato 82094 ungrouped carbonaceous chondrite. *Lunar and Planet. Sci. XLVI Lunar Planet. Inst. Houston*, #2162 (abstr.).

Thangjam G., Nathues A., Mengel K., Hoffmann M., Schäfer M., Reddy V., Cloutis E. A., Christensen M., Sierks H., Le Corre L., Vincent J.-B. and Russell C. T. (2014) Olivine-rich exposures at Bellicia and Arruntia craters on (4) Vesta from Dawn FC. *Meteorit. Planet. Sci.* **49**, 1831–1850.

Thomas R. (2000) Determination of water contents of granite melt inclusions by confocal laser Raman microprobe spectroscopy. *Am. Mineral.* **85**, 868–872.

Udry A., Lunning N. G., McSween H. Y. and Bodnar R. J. (2014) Petrogenesis of a vitrophyre in the Martian meteorite breccia NWA 7034. *Geochim. Cosmochim. Acta* **141**, 281–293.

Ushikubo T., Kimura M. and Kita N. T. (2012) Primordial oxygen isotope reservoirs of the solar nebula recorded in chondrules in Acfer 094 carbonaceous chondrite. *Geochim. Cosmochim. Acta* **90**, 242–264.

Vilas F. (2008) Spectral characteristics of Hayabusa 2 Near-earth asteroid targets 162173 1999 JU3 and 2001 QC34. *Astron. J.* **135**, 1101–1105.

Vilas F. and Gaffey M. J. (1989) Phyllosilicate absorption features in main-belt and outer-belt asteroid reflectance spectra. *Science* **246**, 790–792.

Wasson J. T. and Kallemeyn G. W. (1988) Compositions of chondrites. *Philos. Trans. R. Soc. London* **325**, 535–544.

Wasson J. T., Isa J. and Rubin A. E. (2013) Compositional and petrographic similarities of CV and CK chondrites: a single group with variations in textures and volatile concentrations attributable to impact heating, crushing and oxidation. *Geochim. Cosmochim. Acta* **108**, 45–62.

Weisberg M. K., Ebel D. S., Kimura M., Kita N. T. and Nakashima D. (2010) Petrology and oxygen isotopes of chondrules in the Kota Kota EH3 chondrite. *Lunar and Planet. Sci. XLI Lunar Planet. Inst. Houston*, #1756 (abstr.).

Weisberg M. K., Ebel D. S., Connolly H. C., Kita N. T. and Ushikubo T. (2011) Petrology and oxygen isotope compositions of chondrules in E3 chondrites. *Geochim. Cosmochim. Acta* **75**, 6556–6569.

Wilkening L. L. (1973) Foreign inclusions in stony meteorites—I. Carbonaceous chondritic xenoliths in the Kapoeta howardite. *Geochim. Cosmochim. Acta* **37**, 1985–1989.

Yu Y., Hewins R. H., Clayton R. N. and Mayeda T. K. (1995) Experimental study of high temperature oxygen isotope exchange during chondrule formation. *Geochim. Cosmochim. Acta* **59**, 2095–2104.

Zajacz Z., Halter W., Malfait W. J., Müntener O., Bodnar R. J., Bachmann O., Webster J. D., Ulmer P., Mandeville C. W., Hirschmann M. M. and Morizet Y. (2005) A composition independent quantitative determination of the water content in silicate glasses and silicate melt inclusions by confocal Raman-spectroscopy. *Contrib. Miner. Petrol.* **150**(6), 631–642.

Zolensky M. E., Weisberg M. K., Buchanan P. C. and Mittlefehldt D. W. (1996) Mineralogy of carbonaceous chondrite clasts in HED achondrites and the Moon. *Meteorit. Planet. Sci.* **31**, 518–537.

Zolensky M. E. (1997) Structural water in the Bench Crater chondrite returned from the Moon. *Meteorit. Planet. Sci.* **32**, 15–18.

Zolensky M. E., Mikouchi T., Hagiya K., Ohsumi K., Komatsu M. and Le L. (2015) Evidence for impact shock melting in CM and CI chondrite regolith samples. *Lunar and Planet. Sci. XLVI Lunar Planet. Inst. Houston*, #2261 (abstr.).

Associate editor: Gregory F. Herzog